

## Shock-wave/turbulent boundary-layer interaction with a flexible panel

Laguarda, L.; Hickel, S.; Schrijer, F. F.J.; van Oudheusden, B. W.

**DOI**

[10.1063/5.0179082](https://doi.org/10.1063/5.0179082)

**Publication date**

2024

**Document Version**

Final published version

**Published in**

Physics of Fluids

**Citation (APA)**

Laguarda, L., Hickel, S., Schrijer, F. F. J., & van Oudheusden, B. W. (2024). Shock-wave/turbulent boundary-layer interaction with a flexible panel. *Physics of Fluids*, 36(1), Article 016120. <https://doi.org/10.1063/5.0179082>

**Important note**

To cite this publication, please use the final published version (if applicable). Please check the document version above.

**Copyright**





Other than for strictly personal use, it is not permitted to download, forward or distribute the text or part of it, without the consent of the author(s) and/or copyright holder(s), unless the work is under an open content license such as Creative Commons.

**Takedown policy**

Please contact us and provide details if you believe this document breaches copyrights. We will remove access to the work immediately and investigate your claim.

RESEARCH ARTICLE | JANUARY 10 2024

# Shock-wave/turbulent boundary-layer interaction with a flexible panel

L. Laguarda ; S. Hickel ; F. F. J. Schrijer ; B. W. van Oudheusden 



*Physics of Fluids* 36, 016120 (2024)

<https://doi.org/10.1063/5.0179082>



CrossMark



**APL Machine Learning**  
**Latest Articles Online!**  
**Read Now**



# Shock-wave/turbulent boundary-layer interaction with a flexible panel

Cite as: Phys. Fluids **36**, 016120 (2024); doi: [10.1063/5.0179082](https://doi.org/10.1063/5.0179082)

Submitted: 29 September 2023 · Accepted: 11 December 2023 ·

Published Online: 10 January 2024



View Online



Export Citation



CrossMark

L. Laguarda,<sup>a)</sup> S. Hickel, F. F. J. Schrijer, and B. W. van Oudheusden

## AFFILIATIONS

Department of Flow Physics and Technology, Faculty of Aerospace Engineering, Delft University of Technology, Kluyverweg 1, Delft 2629HS, The Netherlands

<sup>a)</sup> Author to whom correspondence should be addressed: [L.LaguardaSanchez@tudelft.nl](mailto:L.LaguardaSanchez@tudelft.nl)

## ABSTRACT

The dynamic coupling between a Mach 2.0 shock-wave/turbulent boundary-layer interaction (STBLI) and a flexible panel is investigated. Wall-resolved large-eddy simulations are performed for a baseline interaction over a flat-rigid wall, a coupled interaction with a flexible panel, and a third interaction over a rigid surface that is shaped according to the mean panel deflection of the coupled case. Results show that the flexible panel exhibits self-sustained oscillatory behavior over a broad frequency range, confirming the strong and complex fluid–structure interaction (FSI). The first three bending modes of the panel oscillation are found to contribute most to the unsteady panel response, at frequencies in close agreement with natural frequencies of the mean deformed panel rather than those for the unloaded flat panel. This highlights the importance of the mean panel deformation and the corresponding stiffening in the FSI dynamics. The time-averaged flow shows an enlarged reverse-flow region in the presence of mean surface deformations. The separation-shock unsteadiness is enhanced due to the panel motion, leading to higher wall-pressure fluctuations in the coupled interaction. Spectral analysis of the separation-shock location and bubble-volume signals shows that the STBLI flow strongly couples with the first bending mode of the panel oscillation. This is further confirmed by dynamic mode decomposition of the flow and displacement data, which reveals variations in the reverse-flow region that follow the panel bending motion and appear to drive the separation-shock unsteadiness. Low-frequency modes that are not associated with the fluid–structure coupling, in turn, are qualitatively similar to those obtained for the rigid-wall interactions, indicating that the characteristic low-frequency unsteadiness of STBLI coexists with the dynamics emerging from the fluid–structure coupling. Based on the present results, unsteady FSIs involving STBLIs and flexible panels are likely to accentuate rather than mitigate the undesirable features of STBLIs.

© 2024 Author(s). All article content, except where otherwise noted, is licensed under a Creative Commons Attribution (CC BY) license (<http://creativecommons.org/licenses/by/4.0/>). <https://doi.org/10.1063/5.0179082>

## I. INTRODUCTION

A central aspect in the structural design of high-speed systems is long-duration exposure to shock-wave/turbulent boundary-layer interactions (STBLIs). These complex multi-scale flow phenomena exhibit energetic low-frequency motions that impose intermittent and high-amplitude loads on nearby components.<sup>1–3</sup> Lightweight skin panels may resonate under these conditions and potentially break due to vibrational fatigue.<sup>4,5</sup> At hypersonic speeds, STBLIs additionally lead to severe localized heating since local heat transfer rates greatly exceed those associated with attached turbulent boundary layers (TBLs).<sup>6</sup> These thermal effects may further degrade the mechanical properties of aircraft components, thereby becoming more prone to failure. The accurate characterization of dynamic fluid–structure interactions (FSIs) is therefore paramount for the design of next-generation high-speed flight vehicles with expanded operational envelopes.<sup>7,8</sup>

Due to their practical relevance, STBLIs have been extensively investigated since the late 1940s.<sup>9</sup> The wide range of Mach number, Reynolds number, and shock strength covered through experimentation, and more recently, with high-fidelity numerical simulations, has helped shape our fundamental understanding of the relevant flow physics.<sup>10</sup> In the presence of substantial flow separation, it is now well-established that the interaction exhibits a very broad range of energetic frequencies.<sup>3</sup> The high-frequency content is associated with small-scale turbulence, while shear layer dynamics are a major source of unsteadiness at moderate frequencies that promote the mass exchange with the reverse-flow region.<sup>11,12</sup> The lower end of the energetic spectrum, in turn, is related to pulsating motions of the separation bubble and the associated longitudinal excursions of the separation shock.<sup>13,14</sup> The fact that the corresponding mechanisms driving these low-frequency motions remain still unclear, despite the large volume of work,

highlights the complexity of the phenomenon and the need for further fundamental research.

In addition, the extensive literature on STBLIs mostly considers rigid geometries, which are often canonical like flat plates, compression ramps, and steps.<sup>9</sup> Studies involving elastic components, on the other hand, are far more scarce due to the additional complexities in reproducing and characterizing the resulting FSI system with experiments or numerical simulations.<sup>8,15</sup> From the experimental side, recording simultaneous field measurements of the flow and structural displacements is a challenging task.<sup>4</sup> Spottswood *et al.*<sup>16</sup> were among the first to concurrently employ surface pressure measurements and digital image correlation (DIC) to characterize the response of a clamped elastic panel subject to impinging STBLI at Mach 2.0. They observed a strong dynamic coupling between the flow and the panel, with the panel response exhibiting low-frequency content and being highly sensitive to small changes in the shock impingement location. A strong dynamic coupling was also observed by Ahn *et al.*<sup>17</sup> and Musta *et al.*<sup>18</sup> in a Mach 2.0 compression-ramp STBLI over a fully clamped elastic panel. Proper-orthogonal decomposition (POD) of DIC and surface pressure measurements revealed a dominant low-frequency coupling associated with the first bending mode of panel oscillation.<sup>18</sup> More recently, D'Aguanno *et al.*<sup>19</sup> performed simultaneous DIC and particle-image velocimetry (PIV) measurements to investigate the response of a compliant panel subject to impinging STBLI at Mach 2.0, with the panel clamped on the front and rear edges and free on the sides. Their time-record extends for over 400 cycles of the first bending mode, which together with the third bending mode account for over 90% of the variance of the structural displacement field. These two discrete frequencies also appear energetic in the spectra of the separation-shock location, which the authors extracted from the PIV data. Other experimental works on STBLIs over flexible panels include Spottswood *et al.*,<sup>5</sup> Brouwer *et al.*,<sup>20</sup> Tripathi *et al.*,<sup>21,22</sup> and Eitner *et al.*,<sup>23</sup> and they further confirm the aforementioned observations.

The numerical simulation of aeroelastic problems involving STBLIs has also its challenges.<sup>15</sup> Turbulence-resolving strategies are required to properly capture the STBLI dynamics, which determine the unsteady loads on the compliant structure,<sup>24</sup> and fluid and solid domains need to be coupled within a monolithic or partitioned FSI framework.<sup>25</sup> The time-varying solid geometry requires explicit representation within the fluid domain, either with dynamic mesh deformation or via immersed boundary methods (IBMs), and motion and load transfer at the interface is non-trivial when fluid and solid discretizations do not match.<sup>26</sup> As a result, numerical simulations of complex FSI systems are computationally very expensive, which contributes to the limited range of flow conditions and panel response time-records available in the literature.

The first high-fidelity simulation of a TBL over an elastic panel subject to fast-moving shock impingement was performed by Pasquariello *et al.*<sup>27</sup> with a partitioned FSI solver combining large-eddy simulation (LES) of the flow with a finite element (FE) solver for the structure. The work aimed to replicate the experimental results of Daub *et al.*<sup>28</sup> at Mach 3.0. An overall good agreement between numerical and experimental data was found in terms of flow configuration and static panel deflection but not in terms of dynamic behavior. While self-sustained panel motion was obtained in the numerical investigation, experimental results showed a different oscillation frequency and a clear damping. This highlights how challenging it can be

to properly model and resolve these complex FSI systems. Hoy and Bermejo-Moreno<sup>29</sup> further attempted to replicate the experimental results of Daub *et al.*,<sup>28</sup> at Mach 3.0, combining wall-modeled LES and an FE solver with structural damping. The computational savings attained with the wall-model enabled longer integration times, and the resulting dynamic deflection of the panel was in better agreement with the experimental signal than the results of Pasquariello *et al.*<sup>27</sup> The volume of the reverse-flow region was found to increase considerably in the presence of the flexible panel, and the spectral analysis of wall-pressure additionally revealed enlarged excursions of the separation shock. Very recently, Shinde *et al.*<sup>30</sup> explored the effect of one-way vs two-way coupling between impinging STBLI and a fully clamped flexible panel at Mach 4.0. One-way coupling results were obtained by transferring wall-pressure fields from a rigid-wall STBLI simulation to the structural solver to compute the instantaneous panel response. Despite the quantitative discrepancies, an overall qualitative agreement was observed in the panel response for both approaches, namely, a dominant first bending mode of panel oscillation.

The few available studies thus confirm that STBLI efficiently triggers low-order modes of panel vibration; however, questions related to the coupling mechanism, the corresponding modulation of the STBLI dynamics as a result of surface displacements and the particular role of static and dynamic panel deformation remain still open. The interplay between static surface deformation and STBLI has been studied experimentally<sup>31,32</sup> and with RANS models<sup>33</sup> but not with high-fidelity simulations to the authors' knowledge.

In the present study, we perform wall-resolved LES of a Mach 2.0 impinging STBLI over a flexible thin-panel. A partitioned FSI approach with an FE structural solver is employed together with the adaptive reduced-order model of Thari *et al.*<sup>34</sup> to achieve long integration times, that is, more than 90 flow-through times of the full domain length after the initial transient response of the panel. In order to distinguish effects that are caused by the mean panel deformation from those that are caused by dynamic panel motion, we employ the mean panel deflection as a rigid-wall geometry in a second simulation, which is integrated over the same time interval as the coupled case. Results are compared against the baseline configuration, a flat and rigid-wall STBLI at the same flow conditions.

The paper is organized as follows. Sections II and III, respectively, describe the test case and the employed numerical methodology in the present work. Computational results are then presented and analyzed in Sec. IV, which also includes a modal decomposition of flow and displacement data that successfully isolates the main FSI dynamics. The paper is finally concluded in Sec. V.

## II. PROBLEM DEFINITION

The investigated flow geometry is outlined in Fig. 1. It involves an oblique shock wave impinging on a TBL over a compliant panel (the latter shown in red). The free-stream flow is air at Mach number  $M_\infty = 2.0$  and has a stagnation temperature and pressure of  $T_0 = 288$  K and  $p_0 = 356$  kPa, respectively. The 99% velocity-based boundary layer thickness at the inflow plane  $\delta_{0,i}$  is 5.2 mm, and the corresponding Reynolds number based on free-stream quantities,  $Re_\infty = \rho_{F,\infty} u_\infty \delta_{0,i} / \mu_{F,\infty}$ , is  $50.1 \times 10^3$ . Note that subscripts F and S are used to distinguish between fluid and solid variables when necessary. The panel has a thickness  $h = 0.25$  mm and consists of Aluminum 7075-T6, which has a Young's modulus of  $E = 71.1$  GPa, a Poisson ratio of  $\nu = 0.33$ , and a density of  $\rho_{S,0} = 2800$  kg m<sup>-3</sup>. The

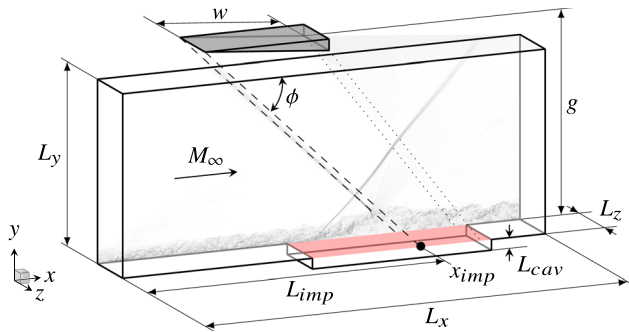


FIG. 1. Schematics of the computational domain.

length of the panel is  $a = 100$  mm, and the panel is clamped at the front and the rear with free side edges. The corresponding non-dimensional dynamic pressure parameter, commonly used in panel flutter studies, is  $\lambda = \rho_{F,\infty} u_{\infty}^2 a^3 D^{-1} = 2440$ , where  $D = Eh^3 / (12(1 - \nu^2))$  is the flexural rigidity of the panel. The flow deflection induced by the shock generator is  $\vartheta = 10.66^\circ$ , which results in an oblique shock wave with a wave angle  $\phi = 40.04^\circ$  and a pressure ratio  $\Pi = 1.76$ . The shock generator is placed at a height  $g = 96$  mm above the surface, while its streamwise position is set such that the theoretical inviscid shock impingement point  $x_{imp}$  occurs at 60% of the panel length and is located  $L_{imp} = 32\delta_{0,i}$  downstream of the inflow plane. The considered channel height to wedge hypotenuse ratio is  $g/w = 1.16$ . Furthermore, a constant pressure of  $1.87p_{\infty}$  is prescribed in the cavity, where  $p_{\infty}$  is the free-stream static pressure of the flow. This value corresponds to the mean wall-pressure of the flat rigid-wall STBLI over the panel.

### III. COMPUTATIONAL METHOD

A partitioned FSI framework with coupled domain-specific solvers is used to advance the system in time. The computational domain in Fig. 1 thus consists of a non-overlapping fluid  $\Omega_F$  and solid  $\Omega_S$  domains with a conjoined interface  $\Gamma = \Omega_F \cap \Omega_S$  (whose normal vector  $\mathbf{n}^\Gamma$  in spatial configuration points into the fluid domain). In the following, when using index notation, the Einstein summation convention in the case of a repeated index is implied unless otherwise stated.

#### A. Fluid

The fluid domain is governed by the three-dimensional compressible Navier–Stokes equations, solved in conservative form

$$\partial_t \mathbf{U} + \nabla \cdot \mathbf{C}(\mathbf{U}) + \nabla \cdot \mathbf{H}(\mathbf{U}) - \nabla \cdot \mathbf{D}(\mathbf{U}) = \mathbf{0} \quad \text{in } \Omega_F, \quad (1)$$

where the state vector  $\mathbf{U} = [\rho_F, \rho_F u_1, \rho_F u_2, \rho_F u_3, \rho_F E]^\top$  consists of the fluid density  $\rho_F$ , the linear momentum  $\rho_F u_i$  for  $i = 1, 2, 3$ , and the total energy  $\rho_F E$ . The total flux in Eq. (1) consists of advection,  $\mathbf{C}$ , pressure terms,  $\mathbf{H}$ , and viscous terms,  $\mathbf{D}$ ,

$$\mathbf{C}_i = u_i \mathbf{U}, \quad \mathbf{H}_i = \begin{bmatrix} 0 \\ \delta_{i1} p \\ \delta_{i2} p \\ \delta_{i3} p \\ u_k \delta_{ik} p \end{bmatrix}, \quad \mathbf{D}_i = \begin{bmatrix} 0 \\ \sigma_{i1} \\ \sigma_{i2} \\ \sigma_{i3} \\ u_k \sigma_{ik} + q_i \end{bmatrix}, \quad (2)$$

where  $u_i$  is the velocity vector and  $(\sigma_{ij})_{i,j=1,2,3}$  is the viscous stress tensor for a Newtonian fluid

$$\sigma_{ij} = \delta_{ij} \lambda_F \partial_k u_k + \mu_F (\partial_j u_i + \partial_i u_j), \quad (3)$$

with  $\mu_F$  being the dynamic viscosity and  $\lambda_F$  being the second viscosity coefficient. Following the Stokes hypothesis, we consider  $\lambda_F = -2/3\mu_F$ , which establishes  $\sigma_{ij}$  as purely deviatoric. The heat flux  $q_i$  is modeled by Fourier's law

$$q_i = \kappa \partial_i T. \quad (4)$$

Static pressure  $p$  and temperature  $T$  of air, which is modeled as a perfect gas, follow from the total energy

$$\rho_F E = \rho_F e + \frac{1}{2} \rho_F u_k u_k, \quad k = 1, 2, 3, \quad (5)$$

and the ideal-gas equation of state

$$p = (\gamma - 1) \rho_F e = \mathcal{R} \rho_F T, \quad (6)$$

where the specific gas constant  $\mathcal{R}$  is taken as  $287.05 \text{ J}(\text{kg K})^{-1}$  and the ratio of specific heats  $\gamma = c_p/c_v = 1.4$ . The thermal conductivity  $\kappa$  is defined as

$$\kappa = \frac{\gamma \mathcal{R}}{(\gamma - 1) Pr} \mu_F, \quad (7)$$

with a constant molecular Prandtl number  $Pr = 0.72$ . The temperature dependency of the dynamic viscosity is modeled as  $\mu_F(T) = \mu_{\infty} \sqrt{T/T_{\infty}}$ .

The fluid domain is solved with the finite-volume solver INCA (<https://www.inca-cfd.com>), which employs the adaptive local deconvolution method (ALDM) for implicit LES of the governing equations.<sup>35</sup> ALDM is a non-linear solution-adaptive finite-volume method that exploits the discretization of the hyperbolic flux  $\mathbf{C} + \mathbf{H}$  to introduce a physically consistent sub-grid scale turbulence model. Since unresolved turbulence and shock waves require fundamentally different modeling, ALDM relies on a shock sensor to control model parameters. This guarantees the accurate propagation of smooth waves and turbulence without excessive numerical dissipation while providing essentially non-oscillatory solutions at strong discontinuities.<sup>35</sup> Gradients in the viscous flux tensor  $\mathbf{D}$  are approximated by linear second-order schemes, and the third-order total variation diminishing Runge–Kutta scheme of Gottlieb and Shu<sup>36</sup> is employed for time integration. The reader is referred to Hickel *et al.*<sup>35</sup> for implementation details of the method and validation results.

The fluid solver operates on block structured, piecewise Cartesian grids. The employed block distribution for the present simulations is shown in Fig. 2. The spatial resolution at the surface is sufficiently high to properly resolve the near-wall turbulence, and a block-wise coarsening in streamwise and spanwise directions is applied away from the surface. The cut-cell immersed boundary method (IBM) of Örley *et al.*<sup>37</sup> and Pasquariello *et al.*<sup>38</sup> is employed in this work to accurately represent the moving panel in the Cartesian fluid domain. A small cavity is therefore added underneath the panel to allow for negative displacements of the moving boundary; see Fig. 2. The grid distribution within the cavity has been generated by mirroring the grid distribution above the cavity around  $y = 0$ .

The discrete panel surface comprises several structural interface elements; see Sec. III B. Each structural element is triangulated, and the

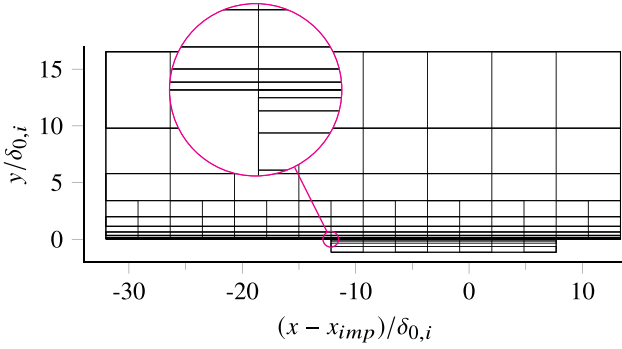


FIG. 2. Block distribution of the employed computational grid.

resulting set of interface triangles  $\Gamma_{tri}$  serves as input to the IBM algorithm. Figure 3 shows a Cartesian computational cell  $\Omega_{i,j,k}$  that is intersected by the triangulated moving surface, which for illustration purposes includes four different interface triangles. A fluid cell that is intersected by at least one interface triangle is referred to as a cut-cell, whereas an interface triangle segment within the cut-cell is a cut-element  $\Gamma_{ele} = \Gamma_{tri} \cap \Omega_{i,j,k}$ . For cut-cells, the integral form of Eq. (1) is then evaluated over the fraction of the cell that belongs to the fluid domain  $\Omega_F$ ,

$$\int_{t^n}^{t^{n+1}} \int_{\Omega_{i,j,k} \cap \Omega_F} \partial_t \mathbf{U} dV dt + \int_{t^n}^{t^{n+1}} \int_{\partial(\Omega_{i,j,k} \cap \Omega_F)} \mathcal{F}(\mathbf{U}) \cdot \mathbf{n} dS dt = 0, \quad (8)$$

and over the time step  $\Delta t = t^{n+1} - t^n$ . The total flux is here denoted  $\mathcal{F}(\mathbf{U})$ , and  $dS$  and  $dV$  indicate the infinitesimal surface and volume elements, respectively. The area integral, which results from the application of the divergence theorem, is taken over the wetted surface of the computational cell, i.e.,  $\partial(\Omega_{i,j,k} \cap \Omega_F)$ . Applying a volume average of the state vector  $\mathbf{U}$ ,

$$\bar{\mathbf{U}}_{i,j,k} = \frac{1}{\alpha_{i,j,k} V_{i,j,k}} \int_{\Omega_{i,j,k} \cap \Omega_F} \mathbf{U} dx dy dz, \quad (9)$$

and considering a forward Euler time integration scheme (for demonstration purposes) yield the following discrete form of Eq. (8):

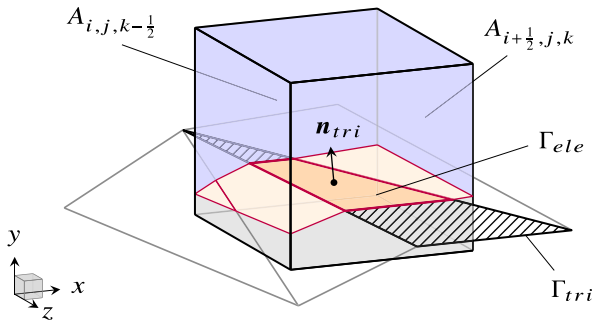


FIG. 3. Schematics of a computational cell intersected by the triangulated moving surface (here shown with four interface triangles).

$$\begin{aligned} \alpha_{i,j,k}^{n+1} \bar{\mathbf{U}}_{i,j,k}^{n+1} &= \alpha_{i,j,k}^n \bar{\mathbf{U}}_{i,j,k}^n + \frac{\Delta t}{\Delta x_i} \left[ A_{i-\frac{1}{2},j,k}^n \mathcal{F}_{i-\frac{1}{2},j,k}^{(1)} - A_{i+\frac{1}{2},j,k}^n \mathcal{F}_{i+\frac{1}{2},j,k}^{(1)} \right] \\ &+ \frac{\Delta t}{\Delta y_j} \left[ A_{i,j-\frac{1}{2},k}^n \mathcal{F}_{i,j-\frac{1}{2},k}^{(2)} - A_{i,j+\frac{1}{2},k}^n \mathcal{F}_{i,j+\frac{1}{2},k}^{(2)} \right] \\ &+ \frac{\Delta t}{\Delta z_k} \left[ A_{i,j,k-\frac{1}{2}}^n \mathcal{F}_{i,j,k-\frac{1}{2}}^{(3)} - A_{i,j,k+\frac{1}{2}}^n \mathcal{F}_{i,j,k+\frac{1}{2}}^{(3)} \right] + \frac{\Delta t}{V_{i,j,k}} \chi_{i,j,k}, \end{aligned} \quad (10)$$

where  $\alpha_{i,j,k}$  is the fluid volume fraction of the cut-cell,  $V_{i,j,k} = \Delta x_i \Delta y_j \Delta z_k$  is the total cell volume,  $A$  is the effective fluid wetted cell-face aperture (indicated in blue in Fig. 3), and  $\mathcal{F}^{(i)}$  is the face-averaged numerical fluxes across the regular cell faces. The interface exchange term  $\chi_{i,j,k} = \sum_{ele} \chi_{ele}$  is added to account for the moving surface  $\Gamma_{i,j,k} = \sum_{ele} \Gamma_{ele}$  within the cut-cell, where  $\sum_{ele}$  indicates the sum over all cut-elements associated with  $\Omega_{i,j,k}$ . The cut-element based interface exchange term  $\chi_{ele}$  accounts for pressure and viscous stresses, interface work, and heat transfer through an individual cut-element. The reader is referred to Örley *et al.*<sup>37</sup> and Pasquariello *et al.*<sup>38</sup> for additional details on the method.

As shown in Fig. 1, the computational domain is rectangular with dimensions  $[L_x, L_y, L_z] = [45, 16.5, 4] \delta_{0,i}$ . The small cavity underneath the flexible panel extends the computational domain a distance  $L_{cav} = \delta_{0,i}$  below the surface of the rigid wall. Nonreflecting boundary conditions are employed at the top and outflow boundaries,<sup>39</sup> and periodicity is imposed in the spanwise direction. The wall (both rigid and flexible segments) is modeled as isothermal at the free-stream stagnation temperature, i.e.,  $T_{wall} = T_0$ . The incident shock and trailing-edge expansion fan are introduced at the top boundary by prescribing far-field conditions based on the Rankine–Hugoniot relations and Prandtl–Meyer theory. At the inflow plane, turbulent boundary conditions with a well-defined space and time correlations are prescribed via the digital filter technique of Xie & Castro.<sup>40</sup> Details about the implementation of the filtering procedure are provided in Laguarda and Hickel,<sup>41</sup> and the employed digital filter settings in the present simulations correspond to those for case A2 in their publication. The target first and second-order statistics at the inflow are derived from the DNS data of Pirozzoli and Bernardini<sup>42</sup> at  $Re_\tau \approx 1000$ .

## B. Solid

The solid domain is governed by the local form of the linear momentum balance, also known as Cauchy's first equation of motion, which in the reference (i.e., undeformed) configuration reads

$$\rho_{S,0} \frac{\partial \mathbf{d}}{\partial t^2} = \nabla_0 \cdot \mathbf{P} + \rho_{S,0} \mathbf{b} \quad \text{in } \Omega_S, \quad (11)$$

where  $\mathbf{d}$  represents the vector of unknown displacements,  $\rho_{S,0}$  is the material density of the solid,  $\nabla_0 \cdot (\cdot)$  is the divergence operator,  $\mathbf{P}$  is the first Piola–Kirchhoff stress tensor, and  $\mathbf{b}$  denotes the external material body forces. The Cauchy stress tensor  $\mathbf{T}$  is related to  $\mathbf{P}$  via

$$\mathbf{T} = \frac{1}{J} \mathbf{P} \cdot \mathbf{F}^T, \quad (12)$$

where  $\mathbf{F}$  is the deformation gradient tensor, which maps a line element in the reference configuration to the current configuration, and  $J = \det(\mathbf{F})$  is the Jacobian of the mapping. Furthermore, and for later reference, the second Piola–Kirchhoff stress tensor  $\mathbf{S}$  is defined as  $\mathbf{S} = \mathbf{F}^{-1} \cdot \mathbf{P}$  and is symmetric, as opposed to  $\mathbf{P}$ .

The constitutive law used in this work is derived from the hyper-elastic Saint Venant–Kirchhoff material model. Its strain energy function  $W$  is defined as

$$W(\mathbf{E}) = \mu_S \mathbf{E} : \mathbf{E} + \frac{1}{2} \lambda_S (\text{tr}(\mathbf{E}))^2, \quad (13)$$

where  $\lambda_S$  and  $\mu_S$  are the first and the second Lamé parameters and  $\mathbf{E}$  is the Green–Lagrange strain tensor, i.e.,

$$\mathbf{E} = \frac{1}{2} (\mathbf{F}^T \cdot \mathbf{F} - \mathbf{I}). \quad (14)$$

The material response is then governed by

$$\mathbf{S} = \frac{\partial W}{\partial \mathbf{E}}, \quad (15)$$

which leads to the employed constitutive law

$$\mathbf{S} = \lambda_S (\text{tr}(\mathbf{E})) \mathbf{I} + 2\mu_S \mathbf{E}. \quad (16)$$

Note that Eq. (16) is analogous to the constitutive relation in linear elasticity and does not reflect material non-linearities (i.e., stress is still linearly related to strain). However,  $\mathbf{E}$  includes geometrical non-linearities and is insensitive to rotation; see Eq. (14).

The principle of virtual work is employed to re-write Eq. (11) in an integral form. This involves the multiplication of the balance equation by the virtual displacement vector  $\delta \mathbf{d}$  and integration over the structural subdomain, which upon some manipulation yields

$$\int_{\Omega_{S;0}} (\rho_{S;0} \ddot{\mathbf{d}} \cdot \delta \mathbf{d} + \mathbf{S} : \dot{\mathbf{E}} - \rho_{S;0} \mathbf{b} \cdot \delta \mathbf{d}) dV_0 - \int_{\partial\Omega_{S;0}} \mathbf{p} \cdot \delta \mathbf{d} dA_0 - \delta W_S^\Gamma = 0, \quad (17)$$

where the divergence theorem is also applied. Note that all integrals are taken over the reference configuration, with  $dA_0$  and  $dV_0$  being the corresponding infinitesimal surface and volume elements. Additionally,  $\dot{\mathbf{E}}$  indicates the variation of the Cauchy stress tensor and  $\mathbf{p}$  denotes the Piola traction.

Equation (17) can be seen as the balance of virtual work, which also includes the work at the FSI interface  $\delta W_S^\Gamma$ . This equation forms the basis for the finite-element method (FEM) in solid mechanics, which is used for the spatial discretization. The solid domain is composed of  $n^e$  elements  $\Omega_S^e$  with consistent basis functions for representing the displacement field. By assembling the contribution of all elements, the semi-discrete form of Eq. (17) is

$$\mathbf{M} \ddot{\mathbf{d}} + \mathbf{f}_{S;\text{int}}(\mathbf{d}) - \mathbf{f}_{S;\text{ext}} - \mathbf{f}_S^\Gamma = \mathbf{0}, \quad (18)$$

where  $\mathbf{M}$  is the mass matrix,  $\mathbf{d}$  and  $\ddot{\mathbf{d}}$  are the discrete vectors of displacements and accelerations, and  $\mathbf{f}_{S;\text{int}}$ ,  $\mathbf{f}_{S;\text{ext}}$ , and  $\mathbf{f}_S^\Gamma$  are the internal, external, and interface force vectors.

Equation (18) is solved with the finite-element solver CalculiX (<http://www.calculix.de>), which uses the Hilbert–Hugues–Taylor  $\alpha$ -method<sup>43</sup> for time discretization. This method is an extension of the Newmark method<sup>44</sup> and allows for some degree of numerical dissipation without degrading accuracy. The parameter  $\alpha$ , which controls the added numerical dissipation, is here set to  $-0.3$ , and the resulting implicit time stepping is solved using a Newton–Raphson method.

The flexible panel is discretized with 20-node hexahedral elements with three degrees of freedom per node (corresponding to the nodal translations in  $x$ ,  $y$ , and  $z$ ). The displacement field within each element is represented with quadratic shape functions. The employed solid mesh consists of 196 elements in the streamwise direction and two elements along its thickness; the panel is restricted to purely two-dimensional motion (no torsion) so only one element is used across the span.

In order to reduce the computational cost, the adaptive reduced-order model (AROM) of Thari *et al.*<sup>34</sup> is employed. The method relies on the linearization of Eq. (18) around a deformed reference state, upon which the number of unknowns is decreased using the mode superposition method<sup>45</sup> with a reduced number of modes.

Consider the Taylor expansion of Eq. (18) around a reference state  $\mathbf{d}_{\text{ref}}$ , which can be either the initial condition or an instantaneous solution at the time of the model re-calibration,

$$\mathbf{M} \ddot{\mathbf{d}}_{\text{ref}} + \mathbf{f}_{S;\text{int}}(\mathbf{d}_{\text{ref}}) - \mathbf{f}_{S;\text{ext}} - \mathbf{f}_S^\Gamma + \mathbf{M}(\ddot{\mathbf{d}} - \ddot{\mathbf{d}}_{\text{ref}}) + \mathbf{K}(\mathbf{d} - \mathbf{d}_{\text{ref}}) = \mathbf{0}, \quad (19)$$

where  $\mathbf{K}(\mathbf{d}_{\text{ref}}) = \partial_{\mathbf{d}} \mathbf{f}_{S;\text{int}}|_{\mathbf{d}_{\text{ref}}}$ . The eigenmodes of the structure are obtained by solving the following eigenvalue problem:

$$\mathbf{K}(\mathbf{d}_{\text{ref}}) \Phi = \mathbf{M} \Phi \Omega^2, \quad (20)$$

where the columns of  $\Phi = [\phi_1, \dots, \phi_m]$  are the orthonormalized (with respect to  $\mathbf{M}$ ) eigenvectors, i.e., natural vibration modes, and  $\Omega = \text{diag}(\omega_1, \dots, \omega_m)$  are the corresponding eigenvalues, i.e., natural vibration frequencies in ascending order. For reduced-order modeling, Eq. (19) is projected onto the modal space spanned by the first  $N_{\text{eig}}$  eigenmodes, where  $N_{\text{eig}}$  is user-defined. This drastically reduces the number of unknowns, as the system is now rank  $N_{\text{eig}}$  in modal space. In order to improve the representation of the load vector in modal space, the modal truncation augmentation (MTA) method is additionally employed,<sup>46</sup> which increases the rank of the reduced system by Eq. (1). Time integration in modal space is then performed with the Newmark method.<sup>44</sup>

Note that constructing and updating the above-described AROM is computationally expensive, whereas applying it is cheap. Therefore, the model is re-calibrated when the solution deviates significantly from the reference configuration, i.e., when the maximum absolute deflection  $\delta d_{\text{max}}$  exceeds a user-defined threshold  $\epsilon$ . This threshold thus provides a compromise between simplicity and accuracy of the solution. The limit case of  $\epsilon = 0$  corresponds to the full non-linear FEM solution, since the projection onto the modal basis is lossless thanks to the MTA (provided that the same time integration scheme is used). For the present simulations,  $N_{\text{eig}}$  is set to ten modes and  $\epsilon$  to 25% of the panel thickness.

### C. Fluid–structure coupling

A loosely coupled serial staggered scheme is employed to advance the FSI system from  $t^n$  to  $t^{n+1} = t^n + \Delta t$ . The scheme follows the classical Dirichlet–Neumann partitioning, where the fluid (Dirichlet partition) inherits displacements from the structure and the structure (Neumann partition) is loaded by the fluid pressure and viscous stresses:

1. At time  $t^n$ , the immersed boundary in the fluid domain is updated with the structural displacements  $\mathbf{d}^{\Gamma;n}$  and velocities  $\dot{\mathbf{d}}^{\Gamma;n}$ .
2. The fluid domain is advanced in time, from  $t^n$  to  $t^{n+1}$ . Interface exchange terms are computed from known structural quantities at time  $t^n$ .
3. Fluid interface tractions  $\boldsymbol{\sigma}_f^{\Gamma;n+1} \cdot \mathbf{n}^{\Gamma;n+1}$  are then transferred to the structural interface elements. For details on the load and motion transfer between the non-matching interface, the reader is referred to Thari *et al.*<sup>34</sup>
4. The solid domain is advanced in time, from  $t^n$  to  $t^{n+1}$ , with the new fluid tractions as additional Neumann boundary condition.
5. Proceed to the next time step.

The time step size  $\Delta t$  is determined by the Courant–Friedrichs–Lewy (CFL) stability condition of the Runge–Kutta method used for the fluid solution. We use  $\text{CFL} \leq 1$  everywhere, which guarantees stability and accuracy of the employed methods.

#### IV. RESULTS AND DISCUSSION

Selected results for the baseline STBLI, the coupled STBLI with the flexible panel, and the STBLI over a rigid panel with the mean deformation of the coupled case are presented and discussed. When necessary, the different configurations will be referred with acronyms that follow from the corresponding panel characteristics. That is, the baseline flat wall, which is equivalent to an undeformed and rigid panel, is referred to as UR, the deformed and rigid wall shaped with the mean panel displacements is DR, and the flexible panel dynamically coupled with the flow is denoted as FC.

All simulations have been integrated for over 90 flow-through times of the full domain length after the corresponding initial transients. The last instantaneous solution of the baseline case served as the initial condition for the coupled simulation, in which the flat panel was allowed to deform. Quantities of interest have been extracted from three-dimensional snapshots, which were recorded at a sampling interval of  $0.5\delta_{0,i}/u_\infty$ , leading to an ensemble of 8200 snapshots per case.

##### A. Undisturbed turbulent boundary layer

In order to characterize the approaching TBL, an additional simulation was conducted on the baseline domain without the incident shock. After an initial transient, flow statistics were collected over 12 flow-through times of the full domain length at a sampling rate of  $\Delta t \approx 2\delta_{0,i}/u_\infty$ . Table I provides a summary of relevant boundary

**TABLE I.** Relevant boundary layer parameters at the inviscid impingement point  $x_{\text{imp}}$  without the shock.

Flow parameters	
$\delta_0$ [mm]	7.15
$\theta$ [mm]	0.61
$H$	3.19
$u_\tau$ [m/s]	21.6
$\rho_w$ [kg/m <sup>3</sup> ]	0.56
$Re_{\delta_0}$	$67.1 \times 10^3$
$Re_\theta$	$5.7 \times 10^3$
$Re_\tau$	1226

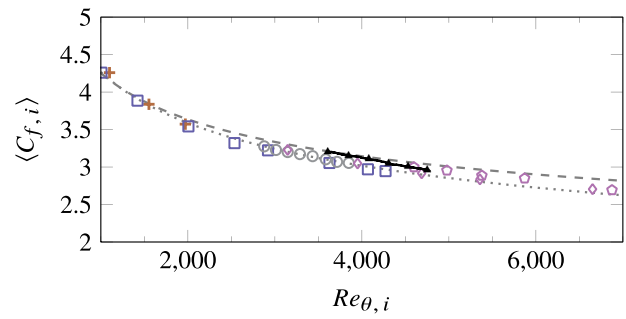
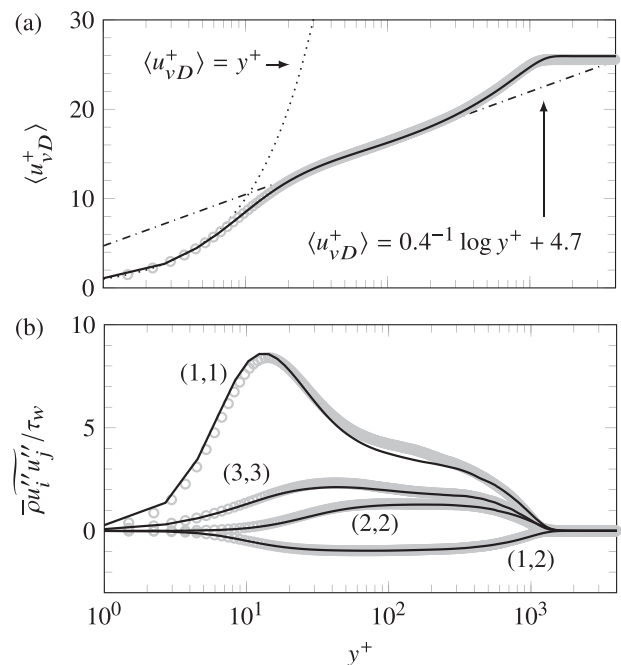


**FIG. 4.** Incompressible skin-friction distribution. Symbol legend: (crosses) Simens *et al.*<sup>47</sup> (squares) Schlatter *et al.*<sup>48</sup> (diamonds, pentagons) Sillero *et al.*<sup>49</sup> (circles) Pirozzoli and Bernardini,<sup>42</sup> (triangles) present LES. Dashed and dotted lines, respectively, denote the incompressible correlations of Schoenherr<sup>50</sup> and Smits *et al.*<sup>51</sup>

layer parameters evaluated at the inviscid impingement point  $x_{\text{imp}}$ , as is commonly done in experiments.

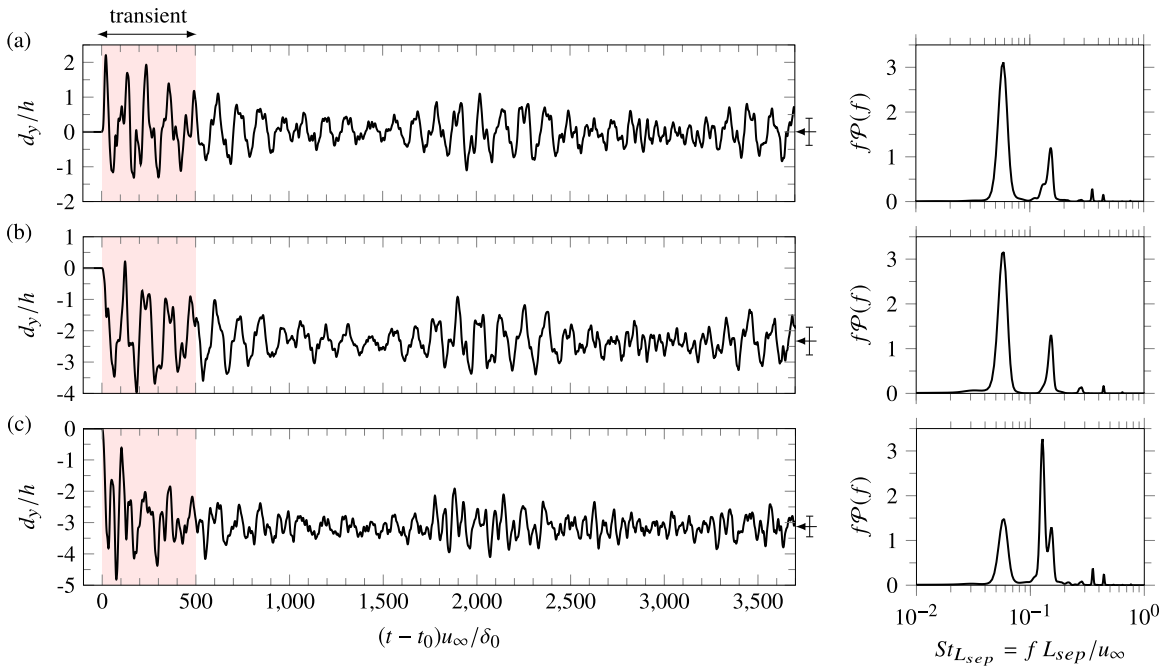
The evolution of the skin-friction coefficient starting from  $5\delta_{0,i}$  downstream of the inflow plane is shown in Fig. 4, where the van Driest II transformation has been employed to remove Mach number effects.<sup>52</sup> As observed, the present LES results agree well with reference incompressible correlations and available DNS data at similar Reynolds numbers.

Figure 5(a) shows the corresponding van Driest-transformed mean streamwise velocity profile evaluated at  $x_{\text{imp}}$ , which is in good agreement



**FIG. 5.** (a) Van Driest-transformed mean streamwise velocity profile, and (b) density-scaled Reynolds stresses at the inviscid impingement location without the shock. Legend: (solid lines) present LES; (symbols) DNS data of Pirozzoli and Bernardini<sup>42</sup> at  $Re_\tau = 1100$ . The indices  $(i, j)$  of the different Reynolds stresses are also indicated in (b).





**FIG. 6.** Instantaneous vertical panel displacements for the (a) quarter point, (b) mid point, and (c) three-quarter point locations along the panel length. Arrows and vertical bars (at the right hand scale) indicate the corresponding mean displacement and its standard deviation. The panels to the right include the pre-multiplied and normalized PSD of the signals.

with the reference DNS data of Pirozzoli and Bernardini<sup>42</sup> for a Mach 2.0 TBL at a comparable  $Re_\tau = 1100$ . Density-scaled Reynolds stresses at the same location are reported in Fig. 5(b) and are also in very good agreement with the reference data. Most notably, the magnitude and position of the stress peaks are well captured in the present LES.

The streamwise spectra (not shown here) have a dominant inner peak at a wavelength  $\lambda_x^+ \approx 700$  and an emerging outer peak at  $\lambda_x \approx 5\delta_0$ . While this is indicative of incipient scale separation, the largest scales in the TBL are still not expected to meaningfully alter the low-frequency dynamics of the investigated STBLI.<sup>3</sup>

### B. Panel response

The time evolution of vertical panel displacements is shown in Fig. 6 for the quarter point, mid point, and three-quarter point

locations along the panel length. The largest displacements are found within the first  $\sim 15$  flow-through times after the flexible panel is released, which corresponds to the initial transient period required to reach the mean deformation state. This initial transient (indicated in red in Fig. 6) is excluded from the statistical analysis. For the remaining simulation time, a self-sustained oscillatory behavior over a broad frequency range is observed, which confirms the strong and complex dynamic coupling between the panel and the flow.

Figure 7(a) shows the mean panel deformation along with the envelope of all instantaneous deflection states after the initial transient. The observed mean shape is consistent with the pressure difference, resulting from the pressure distribution caused by the STBLI on top and the constant imposed cavity pressure at the bottom, and has a maximum downward deflection that exceeds  $3h$  around 70% of the panel length. The corresponding power spectral density (PSD) map of displacements (increasing linearly from white to black) is shown in Fig. 7(b).

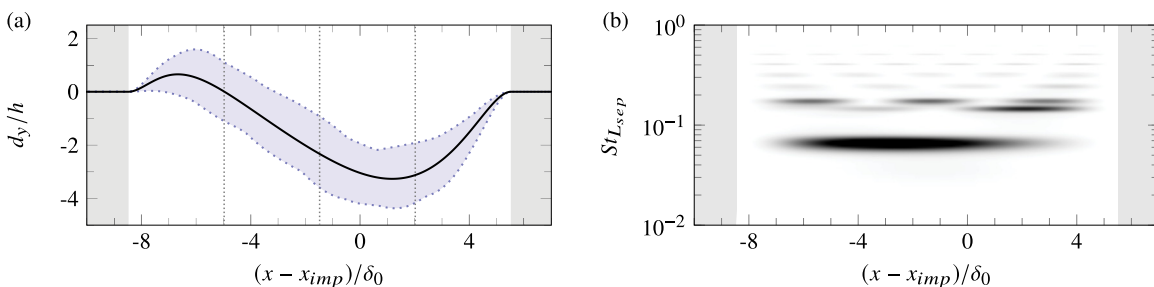


**FIG. 7.** (a) Mean panel deflection (black) together with the envelope of all instantaneous deflection shapes (blue shade), and (b) pre-multiplied PSD map of displacement signals (increasing linearly from white to black). Vertical dotted lines indicate the quarter point, mid point, and three-quarter point locations along the panel length, and the rigid portion of the wall is shaded in gray.

TABLE II. Panel oscillation frequencies.

Natural				Measured	
Flat		Pre-stressed		Hz	$St_{L_{sep}}$
Hz	$St_{L_{sep}}$	Hz	$St_{L_{sep}}$		
134	0.013	538	0.051	593	0.056
375	0.036	1351	0.128	1338	0.127
739	0.070	1554	0.148	1625	0.154

panel displacements is included in Fig. 7(b) and provides an indication of the dominant vibration modes and their respective frequencies. In this work, all PSDs have been estimated using Welch’s algorithm, with Hamming windows and 10 segments with a 65% overlap (segment length of approximately  $650\delta_0/u_\infty$ ).

As shown in Fig. 7(b), the first three bending modes account for most of the variance of the displacement signals, while higher-order modes contribute only marginally. This is in good agreement with previous works.<sup>16,18,19,30</sup> Interestingly, the first bending mode is not symmetric; rather, its largest contribution is found in the second quarter of the panel; see Fig. 7(b). The second bending mode is also highly asymmetric and has energetic contributions predominantly in the second half of the panel. Its frequency is very close to that of the third bending mode, which as opposed to the previous two has a symmetric effect with respect to the panel half-length.

Note that large static displacements increase the effective stiffness of the panel, thereby requiring higher driving frequencies to resonate. Table II reports the first three natural oscillation frequencies for the unloaded flat panel and the pre-stressed deformed panel, which confirm the effective stiffening. These values were obtained with a free-vibration analysis performed with the structural solver, which in the pre-stressed case involved pre-loading the panel with the mean wall-pressure of the coupled simulation. For comparison, Table II also includes the energetic frequencies identified in the displacement signal of the three-quarter point along the panel length [shown in Fig. 6(c) with its corresponding PSD]. These frequencies are in close agreement with natural frequencies of the pre-stressed panel, rather than those for the flat panel, which highlights the importance of mean displacements in the dynamic response of the panel when exposed to STBLI. We also note that the frequency of the first bending mode of the pre-stressed panel lays within the characteristic low-frequency range of STBLI, i.e., a separation-length-based Strouhal number  $St_{L_{sep}} = f L_{sep}/u_\infty$  below 0.1.

### C. Instantaneous and mean-flow organization

An instantaneous impression of the temperature field is provided in Fig. 8 for the coupled interaction to illustrate the investigated STBLI

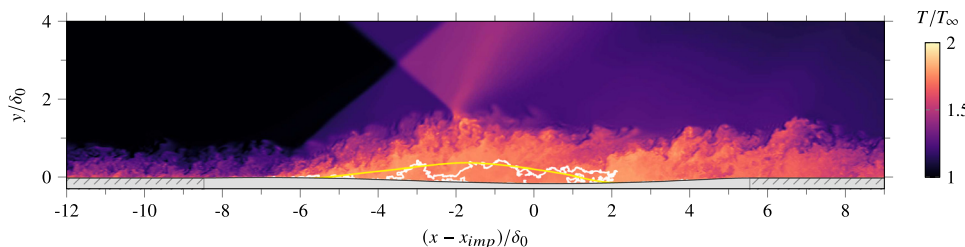
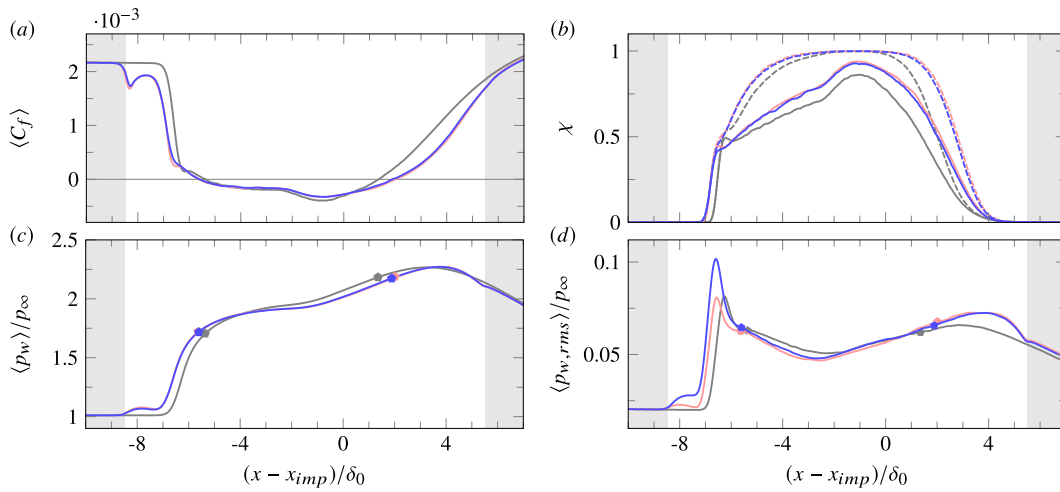


FIG. 8. Instantaneous flow organization of STBLI over the flexible panel. Solid lines indicate instantaneous (white) and mean (yellow) isocontours of zero streamwise velocity. The wall region is colored in gray with stripe patterns highlighting the rigid segments.

topology. Contours of instantaneous (black) and mean (yellow) zero streamwise velocity show the massive flow separation, which is a characteristic of strong interactions. Beyond the separation point, upstream TBL disturbances grow into larger vortical structures as the shear layer moves away from the wall, and they eventually interact with the incident-transmitted shock tip at the bubble apex. Such shock–vortex interaction and the strong flow deceleration near separation correspond to visible peaks in the turbulence kinetic energy (TKE) production.<sup>53</sup> Immediately after the bubble apex, the flow is turned toward the wall and the reattachment process is initiated. All simulations exhibit a very mild concave streamline curvature at reattachment, which results in a weak compression fan instead of a coalesced reattachment shock.

Relevant wall-properties are shown in Fig. 9 to highlight the impact of static and dynamic surface displacements on the flow. Skin-friction distributions in Fig. 9(a) show an increase in 15.6% in the streamwise extent of the reverse-flow bubble for the coupled interaction, shown in blue, with respect to the baseline case, which is indicated in gray. The corresponding separation length  $L_{sep}$ , defined as the streamwise distance between mean separation and reattachment points, increases from  $6.62\delta_0$  to  $7.64\delta_0$  (the separation point moves  $0.42\delta_0$  upstream and the reattachment point moves  $0.61\delta_0$  downstream). The initial skin-friction drop and the partial recovery at the leading edge of the panel are consistent with the upward mean panel deflection at this location; see Fig. 7(a). The following decrease in  $\langle C_f \rangle$ , on the other hand, is attributed to the STBLI and reveals the upstream shift of the separation shock in the presence of the moving panel; see Fig. 9(a). Interestingly, the skin-friction profile for the STBLI over the rigid mean deformed geometry, that is, the DR configuration, is almost identical to that of the coupled interaction, including the magnitude of  $L_{sep}$ , which is  $7.49\delta_0$ . This case is indicated in Fig. 9(a) with a red line. The strong skin-friction similarity between the DR and FC configurations suggests a dominant role of the mean surface deformation on the resulting STBLI organization over a moving panel. This is also confirmed by the probability of reverse-flow in Fig. 9(b), where these two configurations exhibit a very similar increase in reverse-flow probability compared to the baseline.

The corresponding mean and RMS wall-pressure evolution for each configuration are shown in Figs. 9(c) and 9(d). Interestingly, the incipient pressure plateau in the separated region appears more established for the DR and FC configurations in Fig. 9(c), without noticeable differences between the two. A more distinct pressure plateau is generally associated with a stronger interaction,<sup>54</sup> which highlights the impact of the mean surface deformation on STBLI. The dynamic component of panel displacements, in turn, plays an important role in the corresponding wall-pressure fluctuation intensities, which are shown in Fig. 9(d) for all cases. It can be clearly observed that only the FC configuration exhibits a higher peak at the separation-shock foot than



**FIG. 9.** Time- and spanwise-averaged (a) skin-friction, (b) probability of reverse-flow, (c) wall-pressure, and (d) wall-pressure RMS. Line legend: STBLI over a (gray) flat-rigid panel—UR configuration, (red) deformed-rigid panel—DR configuration, and (blue) flexible panel—FC configuration. Pentagon markers denote the corresponding mean separation and reattachment points. Solid and dashed lines in (b) indicate the reverse-flow probability at the wall (solid lines) and considering all points in wall-normal direction (dashed lines). In addition, the rigid-wall segment for the FC configuration is shaded in gray in all panels.

the baseline, being approximately 30% larger. This shows the non-negligible modulation of the separation-shock dynamics due to the moving panel, which leads to a stronger separation-shock footprint on the surface. We will further elaborate on the separation-shock dynamics in the next section. The mean separation-shock location, on the other hand, is still mostly determined by the mean deformation of the panel since wall-pressure fluctuation peaks for the DR and FC configurations are aligned. These configurations also exhibit very similar fluctuation intensities beyond the reattachment location in Fig. 9(d), which are noticeably larger than those for the baseline (UR) interaction.

To better characterize the size of the mean recirculation bubble, different quantities such as its length, height, and volume are reported in Table III for the investigated configurations. In agreement with the above-discussed results, the presented bubble metrics are very similar for the DR and FC configurations, which confirms the strong sensitivity of the separated flow to mean surface deformations. Furthermore, the resulting height and reverse-flow bubble volume for these cases are much closer to the baseline values when considering only  $y \geq 0$ . This suggests that the expansion of the reverse-flow region is primarily a consequence of the mean panel deflection being predominantly

downward; see Fig. 7(a). The two-dimensional probability of reverse-flow is presented in Fig. 10 and shows that the recirculation region is mostly located above a segment of the panel with negative deflection and where the surface curvature is concave. This condition further compresses the flow and contributes to the observed longitudinal expansion of the bubble from both ends.

The influence of static and dynamic panel displacements on the turbulence intensity is analyzed next. Figure 11 shows contours of TKE for the investigated configurations, and all cases exhibit the typical distribution associated with impinging STBLIs.<sup>55</sup> That is, turbulence is first amplified in the detached shear layer, then undergoes a noticeable damping at the bubble apex, and finally re-amplifies again

**TABLE III.** Mean-flow quantities of the recirculation region for the investigated cases.

Flow parameters		UR	DR	FC
Separation length	$L_{sep}/\delta_0$	6.72	7.49	7.64
Bubble height	$H_{sep}/\delta_0$			
• From wall		0.37	0.47	0.47
• From $y = 0$		0.37	0.39	0.39
Bubble volume	$V_{sep}/\delta_0^2 L_z$			
• Integral		1.63	2.43	2.35
• Above $y = 0$		1.63	1.81	1.75

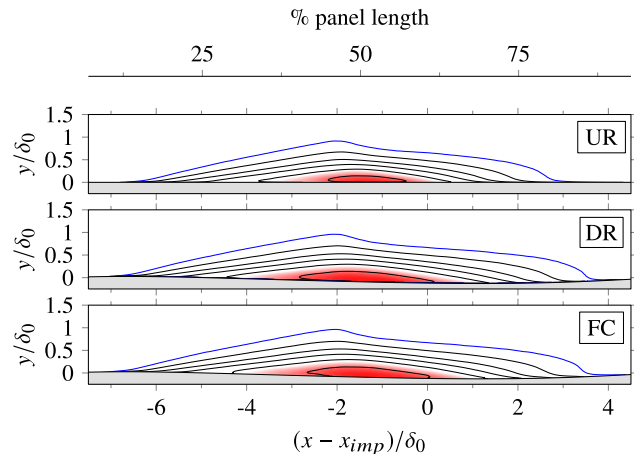


**FIG. 10.** Two-dimensional probability of reverse-flow for (a) the UR configuration, (b) the DR configuration, and (c) the FC configuration. Black lines indicate contour levels from 10% to 90% reverse-flow probability in steps of 20%, while the blue line indicates a 1% contour. For the selected colormap, transition from white to red starts at 75%.

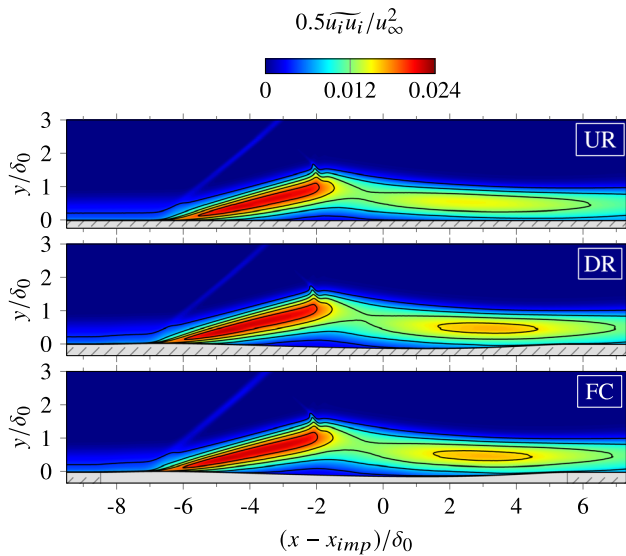


**FIG. 11.** Turbulence kinetic energy (TKE) for the investigated configurations. Black lines correspond to seven equispaced contours, and the wall region is colored in gray with stripe patterns highlighting the rigid segments for each case.

at reattachment. The most noticeable differences are found near and past the reattachment location, where the DR and FC configurations exhibit higher levels of TKE compared to the baseline. This stems from the effective increase in the streamline curvature as a result of the mean downward deflection of the panel and does not appear to be meaningfully altered by the unsteady panel motion.

Table IV reports amplification factors for the TKE and the individual Reynolds stresses. Amplification factors are here defined as the ratio between the maximum value within the interaction region and the maximum value in the undisturbed TBL measured at the inviscid impingement point. For the baseline interaction, that is, the UR configuration, the corresponding factors are in good agreement with previous high-fidelity numerical simulations.<sup>53,56</sup> A comparison of these factors with those associated with the DR and FC configurations then prompts the following observations. First, the maximum TKE amplification does not appear to be meaningfully altered by the resulting mean or dynamic panel displacements. As observed in Fig. 11, this amplification occurs in the detaching shear layer where all cases exhibit a very similar behavior. The same can be said for the amplification of the spanwise Reynolds stress, which also remains effectively unaltered. The wall-normal and shear stress components, on the other hand, undergo approximately 10% higher amplification in the DR and FC

**TABLE IV.** Turbulence amplification factors.

Amplification	UR	DR	FC
$0.5\overline{u_i''u_i''}$	2.60	2.65	2.63
$\overline{u''u''}$	1.97	2.05	2.39
$\overline{v''v''}$	4.35	4.75	4.72
$\overline{w''w''}$	3.57	3.59	3.62
$\overline{u''v''}$	3.97	4.39	4.37

configurations. This amplification is related to the shear layer dynamics close to the reattachment point, which are more intense for these cases. The maximum amplification of the streamwise Reynolds stress is substantially higher in the presence of the moving panel, about 20% larger than in the UR or DR configurations. Inspection of the corresponding transport budgets for this stress reveals enhanced pressure transport at the separation-shock foot (not shown here), which contributes to the additional amplification. As already highlighted in the wall-pressure RMS of Fig. 9(d), the dynamic coupling between the flow and the panel accentuates the separation-shock unsteadiness, which yields a stronger footprint in the pressure fluctuation intensity map of Fig. 12, where the separation shock exhibits increased fluctuation levels as well as a slightly larger longitudinal excursion range in the FC configuration. Figure 12 also highlights the increased shear layer activity near reattachment in the presence of mean surface displacements, with the panel motion having a marginal influence as already discussed.

**D. STBLI dynamics**

In order to identify dominant frequencies contributing to the modulation of the STBLI dynamics as a result of mean and dynamic panel displacements, temporal spectra of wall-pressure, separation-shock location, and bubble-volume variations have been analyzed for the different configurations. For consistency, the separation length  $L_{sep}$  from the baseline interaction is employed in the definition of  $St_{L_{sep}}$  in all cases.

The pre-multiplied and normalized PSD map of wall-pressure in Fig. 13 is considered first. Dashed lines denote the corresponding mean separation and reattachment points for each case, while the leading and trailing edges of the panel are indicated with dotted lines. The excursion range of the separation shock, which is of order  $\delta_0$ , is located in front of the reverse-flow region in all cases and exhibits a distinct low-frequency signature compared to the incoming TBL. In the

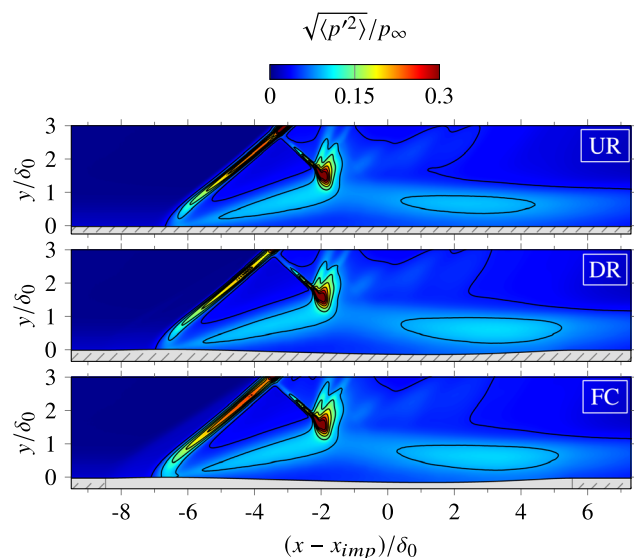


**FIG. 12.** Pressure fluctuation intensity for the investigated configurations. For additional details, see Fig. 11.

25 January 2024 14:13:04

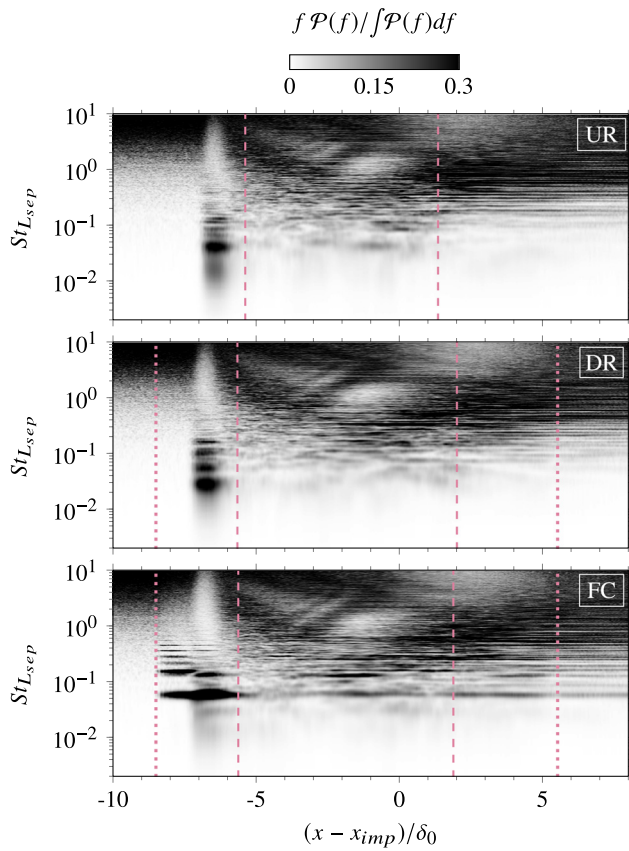


**FIG. 13.** Pre-multiplied and normalized PSD map of wall-pressure along the center-line of the investigated configurations. Dashed lines indicate the mean separation and reattachment locations, and dotted lines mark the leading and trailing edges of the flexible panel.

separated region, the high-frequency content characteristic of small-scale turbulence coexists with moderate frequencies, extending from  $St_{L_{sep}} \approx 1$  to 0.1 and below. The energetic content is centered around  $St_{L_{sep}} \approx 0.5$  near the reattachment location in all cases and then progressively relaxes toward the post-interaction TBL state.

In the presence of both static and dynamic panel displacements, that is, for the DR and FC configurations, the energy density of the low-frequency content is noticeably different compared to the baseline configuration. For instance, the PSD map for the DR configuration exhibits a significant higher harmonic content at the separation-shock foot. This illustrates the non-negligible modulating influence of the deformed surface geometry on the shock unsteadiness. The spectra for the FC configuration, in turn, show that the separation-shock motion resonates with the panel oscillation. The most energetic peaks in the low-frequency range for this configuration correspond to the first and second bending modes of the panel, which are also found energetic upstream of the separation shock range, throughout the reverse-flow region and beyond reattachment. The energetic content associated with the panel motion, particularly at the first bending frequency ( $St_{L_{sep}} \approx 0.056$ ), is also visible downstream of the trailing edge of the panel. This suggests that the dynamic fluid–structure coupling results in pressure disturbances that propagate into the downstream flow.

Further insights on the separation-shock dynamics are obtained by inspecting the time evolution of the separation-shock location signal and its pre-multiplied PSD, which are shown in Fig. 14(a) for the different configurations. Instantaneous shock locations were extracted from the corresponding three-dimensional snapshot sequence by searching for peak values of the pressure gradient field  $|\nabla p|$  in a wall-normal slice outside the boundary layer (at  $y = 1.5\delta_0$ , before intersecting the incident shock) and then averaging the resulting shock front in span. Note that the shock location in Fig. 14(a) is referenced with respect to the mean separation-shock location of the baseline case  $\langle x_{sw}^b \rangle$  for ease of comparison.

In agreement with the analysis in the previous section, the separation shock is clearly located more upstream in the presence of mean

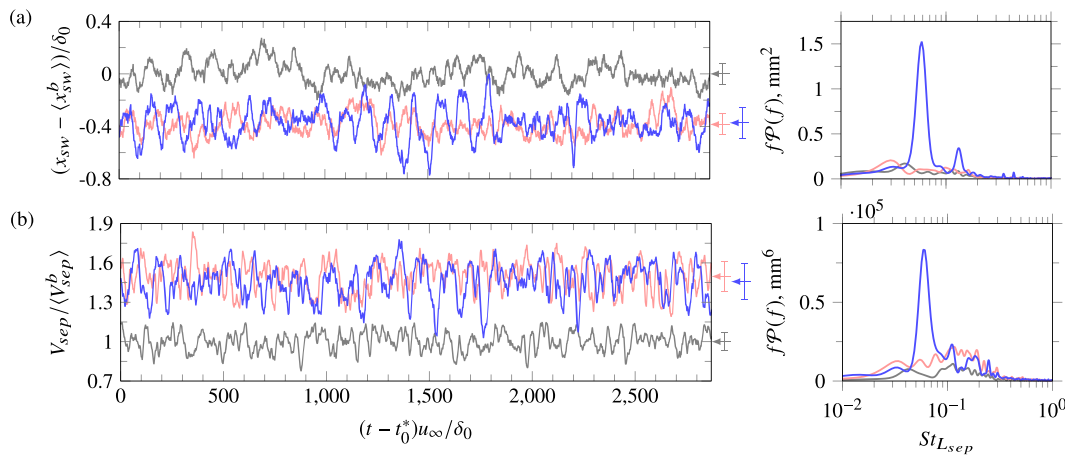


**FIG. 14.** Time evolution of (a) the spanwise-averaged shock position, and (b) separation bubble volume. Color legend: (gray) baseline UR configuration; (red) DR configuration; (blue) FC configuration. The shock position is referenced with respect to the mean shock location of the baseline, i.e.,  $\langle x_{sw}^b \rangle$ , and the bubble-volume signal is normalized with the mean bubble volume of the baseline, i.e.,  $\langle V_{sep}^b \rangle$ . Arrows and vertical bars indicate the corresponding mean value and its standard deviation, and right panels include the pre-multiplied PSD of the signals.

25 January 2024 14:13:04

surface displacements; see the left panel of Fig. 14(a). The arrows on the side, which indicate the mean value of each signal, also make clear that the effect of the panel motion on the mean separation-shock location is secondary to the effect of the mean panel deformation. As observed, the corresponding signals for the DR and FC configurations, which are indicated in red and blue, respectively, have an almost identical mean value. The FC configuration, however, is characterized by noticeably larger excursions of the separation shock from its mean location, which translates into a larger standard deviation of the signal. This is indicated by the vertical bars on the left panel of Fig. 14(a). The present results thus confirm that the excursion domain of the separation shock is effectively increased in the presence of the moving panel, while its mean location is determined by mean (rather than dynamic) surface displacements.

The dominant peak in the corresponding PSD of the separation-shock location signal, shown in the right panel of Fig. 14(a), also confirms that the dynamic FSI coupling is mainly established through the first bending mode of the panel oscillation. The dominant peak of the signal is located at  $St_{L_{sep}} \approx 0.058$ , which is very close to the spectral peak of panel displacements found at  $St_{L_{sep}} \approx 0.056$ ; see Table II. A secondary peak is also visible in the spectra for the coupled case, see Fig. 14(a), at a frequency  $St_{L_{sep}} \approx 0.130$ . This is very close to that of the second bending mode of the panel oscillation, which is found at  $St_{L_{sep}} \approx 0.127$ . Frequencies below the first bending frequency of the panel oscillation are also energetic in the shock location signal of the coupled interaction, and their level is comparable to the low-frequency content of the other configurations (PSDs are not normalized in this figure). This suggests that the low-frequency dynamics characteristic of flat and rigid-wall STBLIs coexist with those emerging from the dynamic coupling with the moving panel, rather than being replaced by them.

We also note that the broadband low-frequency range below the first bending frequency of the panel is centered around  $St_{L_{sep}} \approx 0.03$  for the FC configuration. This peak is aligned with the global spectral peak of the DR configuration, see Fig. 14(a), which further supports the coexistence of FSI and non-FSI low-frequency dynamics in the coupled interaction. Interestingly, the corresponding low-frequency peak for the baseline case is found at  $St_{L_{sep}} \approx 0.04$ . This difference in peak location cannot be accounted by employing the particular  $L_{sep}$  of each configuration, rather than the baseline  $L_{sep}$ , in the definition of its corresponding Strouhal number. As deduced from Table III,  $L_{sep}$  is only about 11%–13% larger in the DR and FC configurations compared to the baseline, which does not account for the observed discrepancy. Our results thus indicate that  $St_{L_{sep}}$  is ineffective in collapsing low-frequency dynamics of flat-wall and deformed-wall STBLIs at the same flow conditions.

The time evolution of the reverse-flow bubble volume is shown in Fig. 14(b), and most of the observed changes in the presence of the flexible panel are in close qualitative agreement with those discussed for the separation-shock location. For ease of comparison, volume signals have also been normalized with the corresponding mean value for the baseline case ( $\langle V_{sep}^b \rangle$ ). As observed, the mean bubble volume increases by approximately 50% in the presence of mean surface displacements, see also Table III, and is not substantially altered by the panel oscillation (if only the fluid domain above  $y=0$  is considered, the increase in bubble volume is 15%). The standard deviation of the bubble-volume signal for the DR configuration, however, is much

closer to that of the FC configuration rather than the baseline. This suggests that bubble dynamics are also largely affected by mean surface displacements. From the corresponding PSDs, shown on the right panel of Fig. 14(b), it is clear that the dominant frequency in the signal for the coupled interaction is also associated with the first bending mode of the panel oscillation. Higher frequencies also appear energetic, but a direct connection with a dominant frequency of panel oscillation cannot be established. We also note that all cases exhibit a peak at  $St_{L_{sep}} \approx 0.1$ , which is global for the UR and DR configurations. In agreement with the observations made in the analysis of the separation-shock unsteadiness, the presence of this common peak indicates that some of the energetic bubble motions are not altered by the surface geometry and coexist with those induced by the considered surface displacements.

## E. Modal analysis

In order to relate global flow phenomena to the energetic frequencies identified in the spectral analysis, we perform dynamic mode decomposition (DMD) of the LES data. DMD is a purely data-driven decomposition technique that seeks to extract  $N$  coherent spatiotemporal structures from a snapshot sequence of length  $N+1$ , i.e.,  $\mathbf{S} = \{\mathbf{s}(t_1), \mathbf{s}(t_2), \dots, \mathbf{s}(t_{N+1})\} \in \mathbb{R}^{M \times (N+1)}$ , yielding

$$\mathbf{s}(t_n) \approx \sum_{i=1}^N \alpha_i \phi_i e^{(\beta + j\omega)n\Delta t}, \quad (21)$$

where  $\alpha_i \in \mathbb{C}$  are the amplitudes of the dynamic modes,  $\phi_i \in \mathbb{C}^M$  are the (unit) modal shapes, and  $\beta, \omega \in \mathbb{R}$  are the corresponding growth rates and oscillation frequencies—see Schmid<sup>57</sup> for further details. Snapshots are considered in single precision to alleviate memory requirements of the decomposition algorithm, and the method described by Sayadi and Schmid<sup>58</sup> is employed to parallelize the calculations.

In the present modal analysis, we use a total of 8200 snapshots per case to produce a modal decomposition with high statistical significance. The considered snapshots, which were recorded at a sampling interval of  $0.68\delta_0/u_\infty$ , include the instantaneous three-dimensional streamwise velocity and pressure fields. For the coupled interaction, panel displacements are also appended to the instantaneous snapshot data so that a statistical link between flow dynamics and panel motion can be established.

The sparsity-promoting DMD algorithm (SPDMD) described by Jovanović *et al.*<sup>59</sup> is employed to seek further dimensionality reduction of the STBLI dynamics. This algorithm facilitates mode selection from the DMD solution by detecting modal flow features that have the strongest influence on the entire snapshot history. For the coupled interaction, our results have so far shown that the STBLI flow strongly resonates with the first bending mode of the panel oscillation. This emerging narrow-banded behavior in an otherwise broadband spectrum makes the investigated FSI particularly suitable for the dimensionality reduction granted by the SPDMD method.<sup>59</sup> The regularization parameter of the SPDMD algorithm is chosen such that the number of retained DMD modes is 41 per case. In addition, and in order to guarantee the statistical significance of the lowest frequencies of the retained modes, we prevent DMD modes with a period of oscillation larger than a third of the total simulation time from being selected by the SPDMD algorithm as dynamically relevant.

Figure 15 shows the corresponding modal amplitudes and frequencies of the resulting DMD modes for each case as well as those retained by the SPDMD algorithm, referred to as SPDMD modes. All modes with non-zero frequencies arise as complex conjugate pairs because the original snapshot data are real-valued. The SPDMD mode set highlights those modes that are dynamically relevant in the DMD solution and that are therefore worth inspecting. These modes are indicated with red crosses in each panel of Fig. 15. The amplitudes of the SPDMD modes are slightly different from the DMD amplitudes because the algorithm recomputes them for an optimal representation of the original data sequence with the retained sparse structure. For the sake of clarity, the spectrum of Fig. 15 only shows Strouhal numbers up to  $St_{L_{sep}} = 0.25$  because this low-frequency range already encompasses the SPDMD mode set of the DR and FC configurations. The corresponding SPDMD solution for the baseline case, on the other hand, contains a few modes with higher oscillation frequencies, up to  $St_{L_{sep}} \approx 0.65$ , which suggests that the lower end of the energetic spectrum of STBLI is more dynamically relevant in the presence of the investigated surface deformations than in the case of a flat wall. We also note that low-frequency modes below  $St_{L_{sep}} = 0.1$  exhibit the largest amplitudes in all cases.

The SPDMD solution of the coupled interaction, see Fig. 15(c), excellently captures the first bending mode of the panel oscillation. The corresponding Strouhal number as measured from the PSD of panel displacements is indicated with a solid blue line in the figure, and it intersects the largest SPDMD modal amplitude with a non-zero frequency almost perfectly. This confirms the excellent capabilities of the SPDMD method in detecting and isolating the main system dynamics. In addition to this tone, the SPDMD solution of the coupled interaction also includes dynamic low-frequency modes below the first bending frequency of the panel oscillation, and their amplitudes are very much in line with the corresponding SPDMD modes of the UR and DR configurations, see Figs. 15(a) and 15(b). This further confirms the observations made in Sec. IV D regarding the emerging FSI dynamics, which coexist with rather than replace the characteristic non-FSI low-frequency dynamics of STBLI. Concerning the higher-order modes of panel oscillation, indicated with dashed lines in Fig. 15(c), the second bending mode also appears to be captured by the SPDMD algorithm in the coupled case. However, it does not emerge as a distinct tone like the first bending mode. The third bending mode

of the panel, in turn, cannot be directly associated with a particular SPDMD mode, indicating that the STBLI flow does not resonate at this frequency.

Based on the above considerations, three SPDMD modes of the coupled interaction are selected and described in the following. These include a representative low-frequency mode below the first bending frequency of the panel oscillation, as well as the dynamic modes closest to the first and second bending frequencies of the panel. Animations of the depicted modal shapes are available in our data repository<sup>60</sup> and should be considered in conjunction with the following discussion.

The selected low-frequency mode below the first bending frequency of the panel oscillation, at  $St_{L_{sep}} \approx 0.015$ , is depicted in Figs. 16(a) and 16(b) at two discrete phase angles,  $\omega_i t = 0$  and  $\omega_i t = \pi/2$ . The associated modal pressure, the modal streamwise velocity, and the modal displacement fields are shown in the left, center, and right panels of the figures, respectively. The modal pressure clearly highlights the connection between the low-frequency unsteadiness of STBLI and longitudinal excursions of the separation shock. These excursions are associated with pressure fluctuations of opposite sign near reattachment, which is consistent with expansions and contractions of the reverse-flow bubble from both ends. The modal streamwise velocity field additionally reveals a statistical link between the low-frequency unsteadiness of the separation shock and streamwise velocity streaks that originate near the separation point. Similar streaks were also identified by Priebe *et al.*<sup>61</sup> in low-frequency DMD modes of a Mach 2.9 compression ramp flow. In agreement with their results, we find that these velocity structures meander in the spanwise direction. The strongest velocity fluctuations are found at the leading edge of the bubble and in the downstream flow, whereas the streak strength is highly damped at the bubble apex due to the interaction with the incident-transmitted shock. This behavior differs therefore from the compression ramp flow case, where an incident shock is absent. The modal displacements show that the panel passively adapts to the pressure variations induced by the oscillating flow. It is important to mention that the low-frequency modes of the UR and DR configurations exhibit qualitatively similar modal shapes as those shown in Fig. 16. This provides further evidence of the coexistence of non-FSI low-frequency dynamics of STBLI with those emerging from the dynamic coupling with the flexible panel.

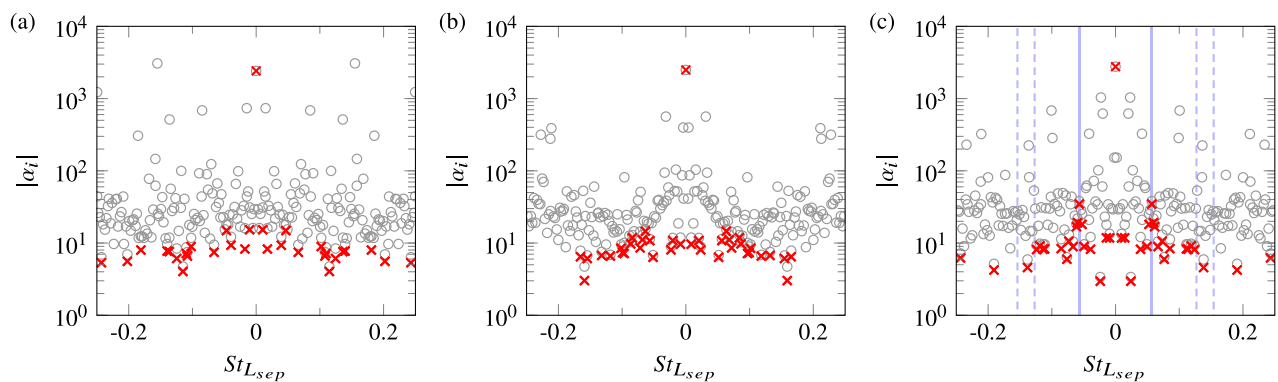
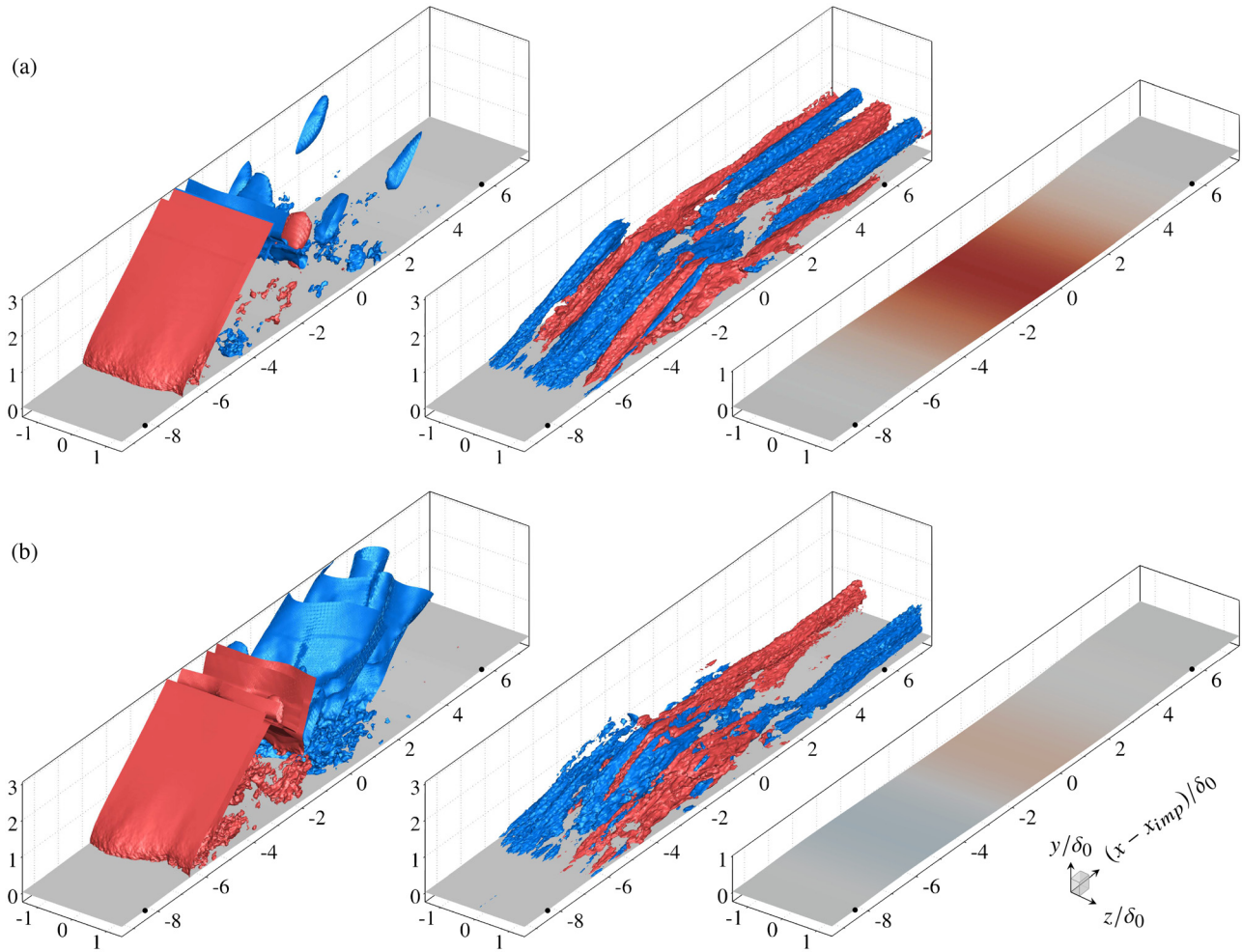


FIG. 15. Dynamic-mode amplitude distribution [i.e.,  $|\alpha_i|$ , see Eq. (21)] for (a) the baseline UR configuration, (b) the DR configuration, and (c) the FC configuration. Symbol legend: (circles) standard DMD solution; (crosses) sparsity-promoting DMD (SPDMD) solution containing 41 modes. Solid blue lines in (c) indicate the first measured bending mode of the panel oscillation, see Table II, while dashed blue lines denote the high-order ones (second and third).



**FIG. 16.** Representative dynamic low-frequency mode of the coupled interaction ( $St_{L_{sep}} \approx 0.015$ ) at two different phase angles: (a)  $\omega_1 t = 0$ , and (b)  $\omega_1 t = \pi/2$ . The different panels include the modal pressure (left), the modal streamwise velocity (center), and the modal displacements (right). Front and rear edges of the flexible panel are indicated with black circles. Iso-contours in the left and center panels indicate strong positive (red) and negative (blue) fluctuations, and the corresponding surface geometry is indicated in gray. In the right panels, the surface geometry is colored by the modal displacements.

Figures 17(a) and 17(b) show two discrete phases of the dynamic mode associated with the first bending frequency of the panel oscillation, with a modal frequency of  $St_{L_{sep}} \approx 0.056$ . The phase difference between both figures is again  $\omega_1 \Delta t = \pi/2$ . This mode differs in many aspects from the low-frequency mode shown in Fig. 16. Most notably, it presents an increased spanwise coherence that is consistent with the two-dimensional motion of the panel. The modal pressure, see the left panels of Fig. 17, exhibits strong fluctuations at the front end of the panel due to the unsteady motion of the upward-deflected leading edge (both edges of the panel are indicated with black circles in the figures). A similar observation can be made for the fluctuations at the trailing edge of the panel, behind the interaction region, where the unsteady bending motion induces pressure disturbances that propagate into the downstream flow. The signature of these structures is also visible in the wall-pressure PSD of Fig. 13. The spanwise coherence of this mode is particularly evident in the modal streamwise velocity field,

which exhibits large-scale fluctuations of the entire shear layer instead of a distinct three-dimensional streak structure. The accompanying modal displacements, which are shown on the right panels of Fig. 17, are clearly asymmetric in the streamwise direction around the panel half-length. This is in agreement with the PSD map of panel displacements shown in Fig. 7(b).

In order to better understand the dynamic coupling at the first bending frequency of the panel, we reconstruct the FSI dynamics by superposing the corresponding SPDMD mode of Fig. 17, hereby referred to as  $\phi_1$ , on the mean mode. Due to the noticeable spanwise coherence of  $\phi_1$ , we consider the spanwise-averaged modal fields and reconstruct the corresponding purely two-dimensional dynamics. When doing so, the amplitude of  $\phi_1$  is amplified by a factor 2 to also account for the effect of its complex conjugate on the mean flow. The resulting reconstructed velocity field is shown on the left panels of Fig. 18 at four equally spaced phase angles, such that Figs. 18(a) and 18(c) correspond



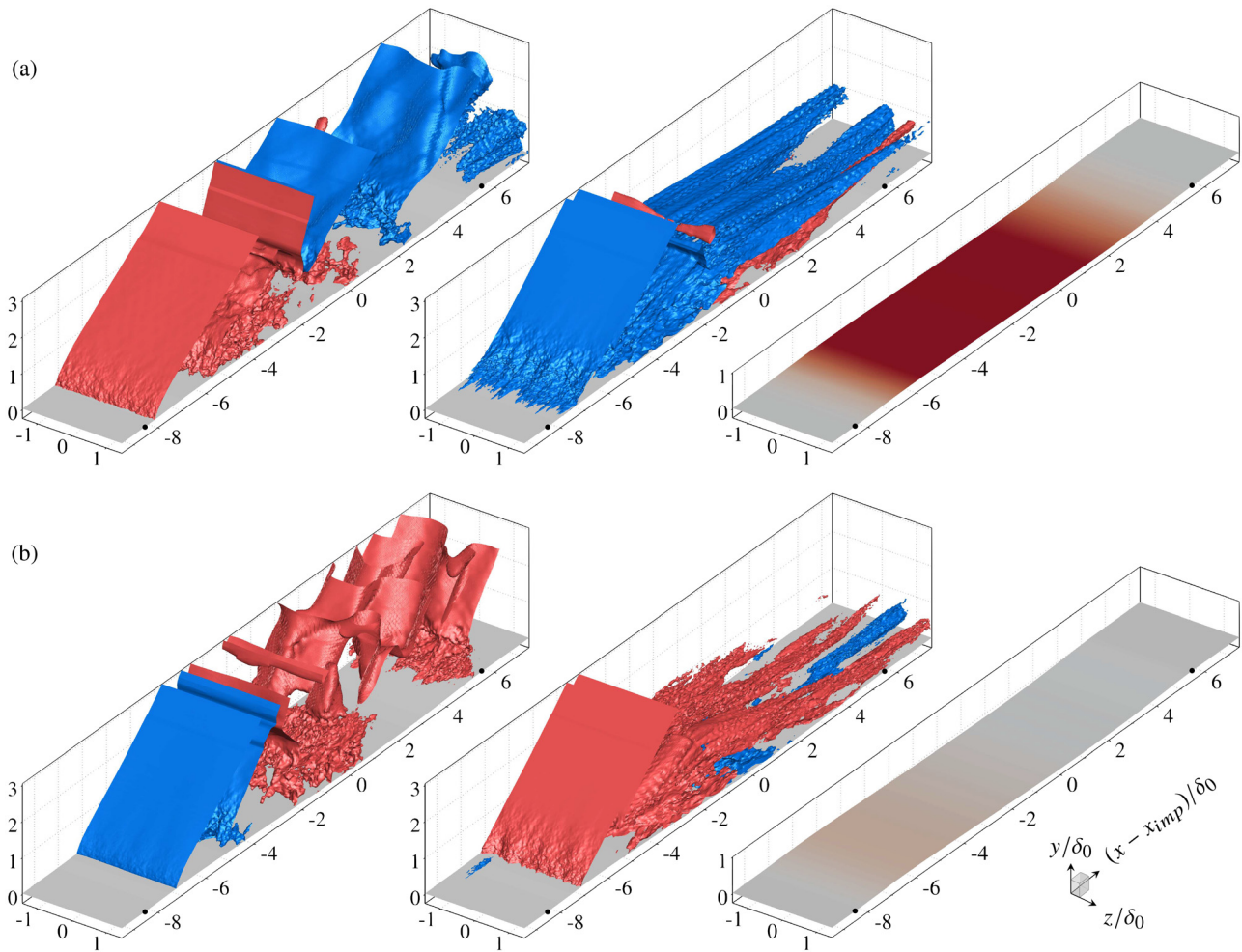
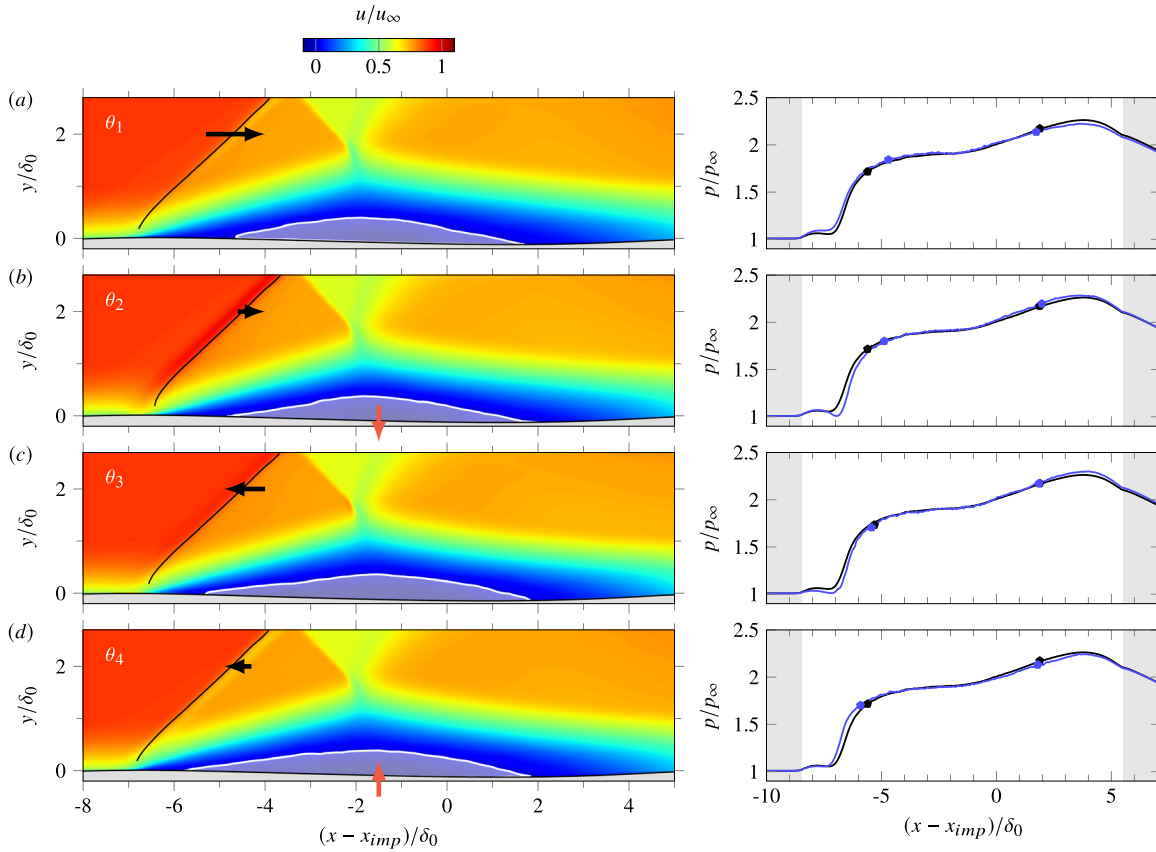


FIG. 17. Dynamic mode associated with the first bending mode of the panel oscillation ( $St_{L_{sep}} \approx 0.056$ ). The phases portrayed in (a) and (b) correspond to phases  $\theta_1$  and  $\theta_2$  in Fig. 19, respectively. For additional details, see Fig. 16.

to the maximum and minimum deflections of the centerpoint of the panel, while Figs. 18(b) and 18(d) depict the intermediate phases. For clarity, the separation shock and the reverse-flow region are indicated with solid lines, and arrows are used to mark the direction of the separation shock and the panel bending motion. The right panels of Fig. 18 include the corresponding variation of the reconstructed wall-pressure (blue line) together with the mean wall-pressure (black line) for reference. The discussion of Fig. 18 should be considered in conjunction with Fig. 19, which shows the corresponding evolution of the mid point displacement of the panel, the separation-shock location, the volume of the reverse-flow bubble, and the integral panel load. Note that the equally spaced phases shown in Figs. 18(a)–18(d), labeled  $\theta_1$ – $\theta_4$ , are also indicated in Fig. 19.

The reconstructed velocity field in Fig. 18 reveals that the reverse-flow bubble volume lags behind the bending motion of the panel by approximately  $\pi/2$ . In a hypothetical very slow oscillation (i.e., quasi-steady), one would expect that the most downward deflection of the panel would lead to the largest reverse-flow bubble volume since the

mean-flow of the coupled case shows an enlarged bubble in the presence of mostly-downward mean surface displacements compared to the baseline interaction, see Sec. IV C. The unsteady nature of the coupling, however, introduces a phase offset between both signals that is particularly evident in Fig. 19(a) (compare solid and dotted lines). As indicated by the dashed blue line of Fig. 19(a), the separation-shock motion is also characterized by asymmetric excursions around its mean location, with larger upstream excursions that persist for less than half of the period. Figure 19(a) also indicates that the separation-shock location signal is approximately anti-correlated with the reverse-flow bubble volume, which is expected considering that the first bending frequency of the panel oscillation is found within the broadband low-frequency range of STBLI.<sup>62,63</sup> The cross correlation between the bubble volume and the separation-shock location signals, however, reveals a small negative time lag between the two. This time lag is visible in Fig. 19(a) and indicates that the shock motion is preceded by variations in the extent of the recirculation region. Interestingly, we find that the observed time lag corresponds precisely to the time



**FIG. 18.** Reconstructed streamwise velocity field based on the mean flow plus the spanwise-averaged dynamic mode corresponding to the first bending frequency of the panel oscillation. The selected phases within one cycle, which are labeled on the left corner of each contour map, are indicated in Fig. 19. The instantaneous separation-shock front is delineated with a black line, and a white line delimits the reverse-flow region (which is also shaded in white). Black and red arrows indicate the direction of separation-shock and panel motion, respectively. The corresponding reconstructed instantaneous wall-pressure (blue) together with its mean distribution (black) are shown on the right panels, where markers indicate separation and reattachment points.

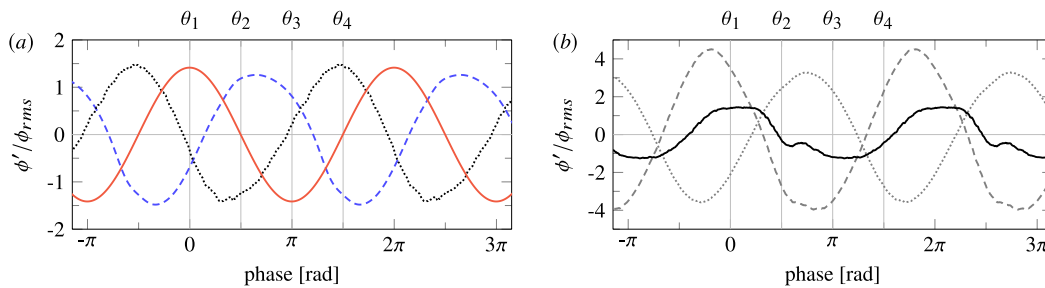


**FIG. 19.** Fluctuations of different quantities for the pure oscillation based on the spanwise-averaged dynamic mode associated with the first bending frequency of the panel oscillation: (a) evolution of the mid point displacement (solid red), the separation-shock location (dashed blue), and the reverse-flow bubble volume (dotted black); (b) evolution of the integrated load over the full panel (solid black) and contributions over the first half (dashed gray) and over the second half of the panel (dotted gray). Four different phases within one cycle are indicated at the top, and they correspond to the reconstructed fields shown in Fig. 18.

required by a pressure disturbance generated at the mean reattachment location to reach the separation line, i.e.,  $\Delta t \approx L_{sep}/a_w$ , where  $a_w$  is the speed of sound at the wall. This finding could support the hypothesis that a downstream instability is the main driver of the separation-shock unsteadiness.<sup>3</sup>

Another relevant element in the considered fluid–structure coupling is the panel load. Together with the resulting elastic forces and the considered cavity pressure, the panel load ultimately drives the panel motion. Figure 19(b) shows the evolution of the integral panel load within the cycle (black solid line), which also presents an

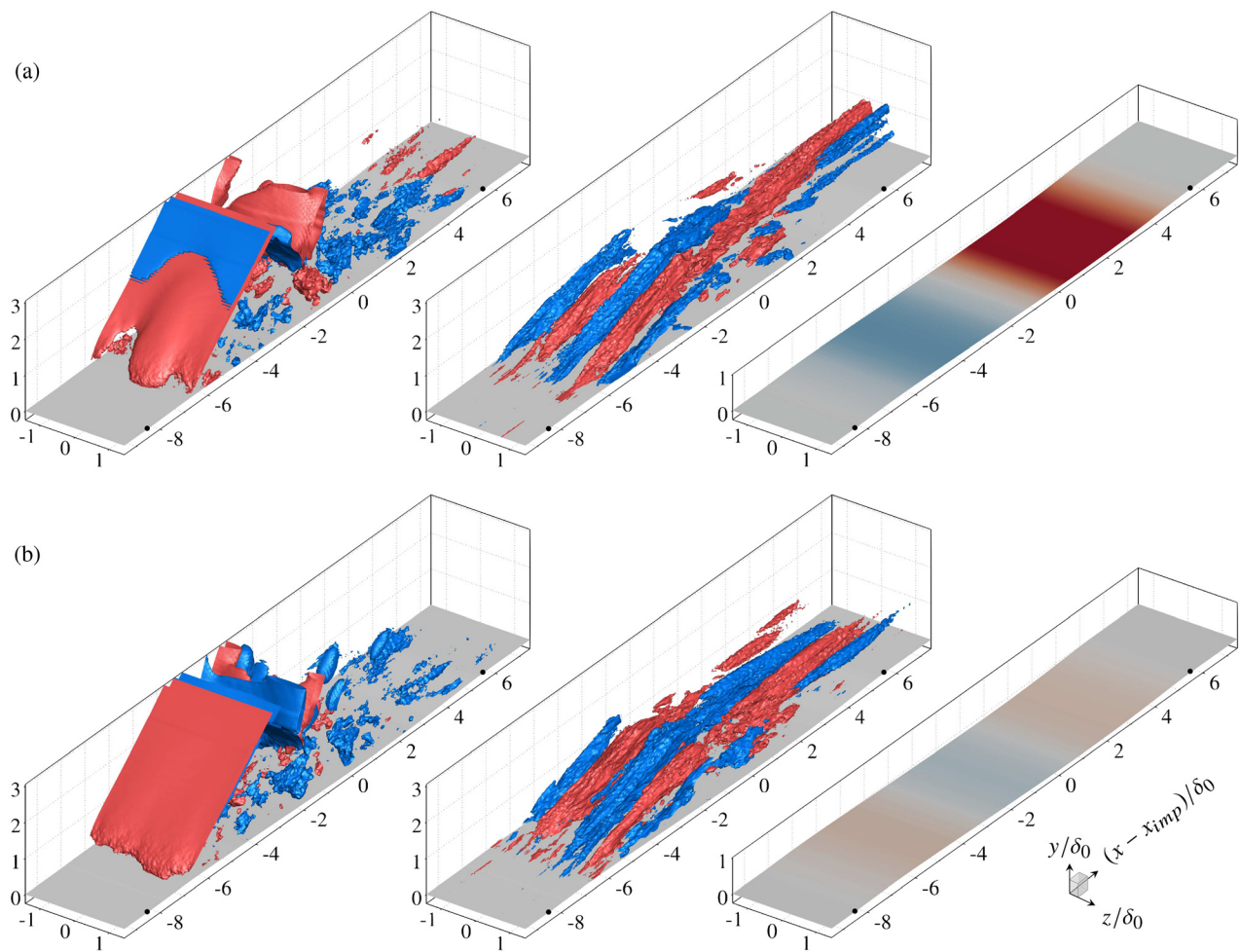


FIG. 20. Dynamic mode associated with the second bending mode of the panel oscillation ( $St_{L_{sep}} \approx 0.124$ ). For additional details, see Fig. 16.

asymmetric behavior around its mean value. The panel load on the first and second halves of the panel, which together constitute the integral panel load, are also indicated in Fig. 19(b) as dashed and dotted gray lines, respectively. By comparing Figs. 19(a) and 19(b), it is clear that the separation-shock location determines the load on the first half, while the trailing edge of the bubble, that is, the reattachment process, influences the load on the second half. The particular evolution of these signals, as well as their relative offset, leads to an integral panel load that essentially increases during the upward bending and decreases during the downward bending, see Fig. 19(b). This is characteristic of a restoring load.

Figure 20 shows a dynamic mode with a characteristic frequency of  $St_{L_{sep}} \approx 0.124$ , which is very close to the second bending frequency of the panel oscillation, see Table II. Qualitatively, the flow characteristics of this mode appear similar to those of the low-frequency mode included in Fig. 16. Differences are mainly found in the modal pressure at the separation shock, which is characterized by narrower longitudinal excursions, noticeable variations in shock deflection, and increased spanwise shock wrinkling. The corresponding modal displacements have an asymmetric effect around the panel half-length with larger

fluctuations in the second half of the panel. This behavior is consistent with the PSD map of panel displacements in Fig. 7(b). Since the first and second halves of the panel also oscillate with a different phase within the mode, the observed asymmetry makes the oscillation at times reminiscent of a third bending mode. We also note that the other configurations exhibit similar modal shapes for the flow variables around this frequency (not shown here), which suggests that the STBLI flow is only weakly coupled with this bending mode.

## V. CONCLUSIONS

Numerical simulations have been performed to investigate the fluid–structure interaction (FSI) between a Mach 2.0 turbulent boundary layer flow, an oblique impinging shock wave, and a flexible panel. The different effects of the mean and dynamic panel displacements on the shock-wave/turbulent boundary-layer interaction (STBLI) dynamics have been assessed by employing the mean panel deflection as a rigid-wall geometry in a second simulation. In addition, results have been compared with a flat rigid-wall STBLI at the same flow conditions.

Our simulation results show that the flexible panel exhibits self-sustained oscillatory behavior over a broad frequency range, confirming the strong and complex dynamic coupling with the flow. The first three bending modes of the panel oscillation are found to represent most of the unsteady panel response. The corresponding modal frequencies appear in close agreement with natural oscillation frequencies of the pre-stressed panel, which are significantly higher than those for the unloaded flat configuration. This highlights the importance of mean surface displacements in the investigated FSI, which need to be accurately captured for a reliable prediction of the dynamic response of the panel. Furthermore, we find that the mean panel deflection causes an enlarged reverse-flow region, while the dynamic panel motion around the mean deflection has a negligible influence on the mean bubble volume. The separation-shock unsteadiness, however, is enhanced by the panel motion, which results in higher wall-pressure fluctuations at its foot. Spectral analysis of the separation-shock location and bubble volume shows that the FSI coupling is mainly established through the first bending mode of the panel oscillation. This is further confirmed by the sparsity-promoting dynamic mode decomposition of the flow and displacement data. Analysis of the low-order modal reconstruction of the FSI reveals variations in the reverse-flow region that follow the panel bending motion and drive the separation-shock unsteadiness. The response of the STBLI flow to surface displacements alters the panel load, which consequently affects the panel motion and sustains the dynamic coupling. Low-frequency modes that are not associated with the fluid–structure coupling, in turn, are very similar to those obtained for the rigid-wall interactions. This indicates that the STBLI dynamics emerging from the unsteady FSI coexist with, rather than replace, the characteristic low-frequency (non-FSI) content of the interaction.

Based on the present results, it is clear that dynamic FSIs involving STBLIs and flexible panels can accentuate the undesirable features of STBLIs. Even though results may vary depending on the impingement location, the interaction strength, or the cavity pressure, the use of flexible structural components as passive flow control devices (as hypothesized in the literature) is not supported by the present findings.

## ACKNOWLEDGMENTS

We acknowledge PRACE (Partnership for Advanced Computing in Europe AISBL) for awarding us access to HAWK at the High-Performance Computing Center Stuttgart, Germany (No. 2020225421).

## AUTHOR DECLARATIONS

### Conflict of Interest

The authors have no conflicts to disclose.

### Author Contributions

**L. Laguarda:** Conceptualization (equal); Data curation (equal); Formal analysis (equal); Funding acquisition (equal); Investigation (equal); Methodology (equal); Project administration (equal); Software (equal); Validation (equal); Visualization (equal); Writing – original draft (equal); Writing – review & editing (equal). **S. Hickel:** Conceptualization (equal); Funding acquisition (equal); Investigation (equal); Methodology (equal); Project administration (equal); Software (equal); Supervision (equal); Validation (equal); Writing – review & editing (equal). **F. F. J. Schrijer:** Investigation (equal); Supervision (equal);

Writing – review & editing (equal). **B. W. van Oudheusden:** Investigation (equal); Supervision (equal); Writing – review & editing (equal).

## DATA AVAILABILITY

The data that support the findings of this study are available within the article and its supplementary material.

## REFERENCES

- <sup>1</sup>P. Dupont, C. Haddad, and J. F. Debieve, “Space and time organization in a shock-induced separated boundary layer,” *J. Fluid Mech.* **559**, 255–277 (2006).
- <sup>2</sup>J. Dély and J.-P. Dussauge, “Some physical aspects of shock wave/boundary layer interactions,” *Shock Waves* **19**, 453 (2009).
- <sup>3</sup>N. T. Clemens and V. Narayanaswamy, “Low-frequency unsteadiness of shock wave/turbulent boundary layer interactions,” *Annu. Rev. Fluid Mech.* **46**, 469–492 (2014).
- <sup>4</sup>A. Gogulapati, R. Deshmukh, A. R. Crowell, J. J. McNamara, V. Vyas, X. Q. Wang, M. Mignolet, T. Bebernis, S. M. Spottswood, and T. G. Eason, “Response of a panel to shock impingement: Modeling and comparison with experiments,” AIAA Paper No. 2014-0148, 2014.
- <sup>5</sup>S. M. Spottswood, T. J. Bebernis, T. G. Eason, R. A. Perez, J. M. Donbar, D. A. Ehrhardt, and Z. B. Riley, “Exploring the response of a thin, flexible panel to shock-turbulent boundary-layer interactions,” *J. Sound Vib.* **443**, 74–89 (2019).
- <sup>6</sup>R. D. Blevins, I. Holehouse, and K. R. Wentz, “Thermoacoustic loads and fatigue of hypersonic vehicle skin panels,” *J. Aircraft* **30**, 971–978 (1993).
- <sup>7</sup>B. Kulfan, “Reynolds numbers considerations for supersonic flight,” AIAA Paper No. 2002-2839, 2002.
- <sup>8</sup>T. G. Eason and S. Spottswood, “A structures perspective on the challenges associated with analyzing a reusable hypersonic platform,” AIAA Paper No. 2013-1747, 2013.
- <sup>9</sup>D. S. Dolling, “Fifty years of shock-wave/boundary-layer interaction research: What next?,” *AIAA J.* **39**, 1517–1531 (2001).
- <sup>10</sup>D. V. Gaitonde, “Progress in shock wave/boundary layer interactions,” *Prog. Aerosp. Sci.* **72**, 80–99 (2015).
- <sup>11</sup>S. Piponniau, J.-P. Dussauge, J.-F. Debieve, and P. Dupont, “A simple model for low-frequency unsteadiness in shock-induced separation,” *J. Fluid Mech.* **629**, 87–108 (2009).
- <sup>12</sup>P. Dupont, S. Piponniau, and J. P. Dussauge, “Compressible mixing layer in shock-induced separation,” *J. Fluid Mech.* **863**, 620–643 (2019).
- <sup>13</sup>V. Pasquariello, S. Hickel, and N. A. Adams, “Unsteady effects of strong shock-wave/boundary-layer interaction at high Reynolds number,” *J. Fluid Mech.* **823**, 617–657 (2017).
- <sup>14</sup>L. Laguarda, S. Hickel, F. F. J. Schrijer, and B. W. van Oudheusden, “Reynolds number effects in shock-wave/turbulent boundary-layer interactions,” *J. Fluid Mech.* (to be published 2024).
- <sup>15</sup>J. J. McNamara and P. P. Friedmann, “Aeroelastic and aerothermoelastic analysis in hypersonic flow: Past, present, and future,” *AIAA J.* **49**, 1089–1122 (2011).
- <sup>16</sup>S. Spottswood, T. Eason, and T. Bebernis, “Influence of shock-boundary layer interactions on the dynamic response of a flexible panel,” in Proceedings of the International Conference on Noise and Vibration Engineering ISMA (2012), pp. 603–616.
- <sup>17</sup>Y.-J. Ahn, M. A. Eitner, M. N. Musta, J. Sirohi, N. T. Clemens, and S. Rafati, “Experimental investigation of flow-structure interaction for a compliant panel under a Mach 2 compression-ramp,” AIAA Paper No. 2022-0293, 2022.
- <sup>18</sup>M. N. Musta, Y.-J. Ahn, M. A. Eitner, J. Sirohi, and N. Clemens, “Unsteadiness in shock/boundary-layer interaction over a compliant panel at Mach 2,” AIAA Paper No. 2022-4136, 2022.
- <sup>19</sup>A. D’Aguanno, P. Quesada Allerhand, F. F. J. Schrijer, and B. W. van Oudheusden, “Characterization of shock-induced panel flutter with simultaneous use of DIC and PIV,” *Exp. Fluids* **64**, 15 (2023).
- <sup>20</sup>K. R. Brouwer, R. A. Perez, T. J. Bebernis, S. M. Spottswood, and D. A. Ehrhardt, “Experiments on a thin panel excited by turbulent flow and shock/boundary-layer interactions,” *AIAA J.* **59**, 2737–2752 (2021).

- <sup>21</sup>A. Tripathi, L. Mears, K. Shoele, and R. Kumar, "Oblique shockwave boundary layer interactions on a flexible panel at Mach 2," AIAA Paper No. 2020-0568, 2020.
- <sup>22</sup>A. Tripathi, J. Gustavsson, K. Shoele, and R. Kumar, "Fluid structure interaction on a compliant panel subject to shock boundary layer interaction," AIAA Paper No. 2021-2806, 2021.
- <sup>23</sup>M. A. Eitner, Y.-J. Ahn, M. N. Musta, J. Sirohi, and N. Clemens, "Effect of ramp-induced shock/boundary layer interaction on the vibration of a compliant panel at Mach 5," AIAA Paper No. 2023-0081, 2023.
- <sup>24</sup>B. Morgan, K. Duraisamy, N. Nguyen, S. Kawai, and S. K. Lele, "Flow physics and RANS modelling of oblique shock/turbulent boundary layer interaction," *J. Fluid Mech.* **729**, 231–284 (2013).
- <sup>25</sup>Y. Bazilevs, K. Takizawa, and T. E. Tezduyar, *Computational Fluid-Structure Interaction: Methods and Applications* (John Wiley & Sons, 2013).
- <sup>26</sup>A. de Boer, A. H. van Zuijlen, and H. Bijl, "Review of coupling methods for non-matching meshes," *Comput. Methods Appl. Mech. Eng.* **196**, 1515–1525 (2007).
- <sup>27</sup>V. Pasquariello, S. Hickel, N. A. Adams, G. Hammerl, W. A. Wall, D. Daub, S. Willems, and A. Gülhan, "Coupled simulation of shock-wave/turbulent boundary-layer interaction over a flexible panel," in 6th European Conference for Aerospace Sciences, 2015.
- <sup>28</sup>D. Daub, S. Willems, and A. Gülhan, "Experiments on the interaction of a fast-moving shock with an elastic panel," *AIAA J.* **54**, 670–678 (2016).
- <sup>29</sup>J. F. Hoy and I. Bermejo-Moreno, "Numerical study of STBLI on flexible panels with wall-modeled LES," AIAA Paper No. 2021-0250, 2021.
- <sup>30</sup>V. Shinde, J. McNamara, and D. Gaitonde, "Dynamic interaction between shock wave turbulent boundary layer and flexible panel," *J. Fluids Struct.* **113**, 103660 (2022).
- <sup>31</sup>M. C. Neet and J. M. Austin, "Effects of surface compliance on shock boundary layer interaction in the Caltech Mach 4 Ludwig tube," AIAA Paper No. 2020-0816, 2020.
- <sup>32</sup>R. Ravichandran, M. Gramola, and P. J. Bruce, "Simultaneous pressure and displacement measurements on a 3D flexible surface in a supersonic flow," AIAA Paper No. 2020-0315, 2020.
- <sup>33</sup>K. R. Brouwer, A. Gogulapati, and J. J. McNamara, "Interplay of surface deformation and shock-induced separation in shock/boundary-layer interactions," *AIAA J.* **55**, 4258–4273 (2017).
- <sup>34</sup>A. Thari, V. Pasquariello, N. Aage, and S. Hickel, "Adaptive reduced-order modeling for non-linear fluid-structure interaction," *Comput. Fluids* **229**, 105099 (2021).
- <sup>35</sup>S. Hickel, C. P. Egerer, and J. Larsson, "Subgrid-scale modeling for implicit large eddy simulation of compressible flows and shock-turbulence interaction," *Phys. Fluids* **26**, 106101 (2014).
- <sup>36</sup>S. Gottlieb and C.-W. Shu, "Total variation diminishing Runge-Kutta schemes," *Math. Comput.* **67**, 73–85 (1998).
- <sup>37</sup>F. Örley, V. Pasquariello, S. Hickel, and N. A. Adams, "Cut-element based immersed boundary method for moving geometries in compressible liquid flows with cavitation," *J. Comput. Phys.* **283**, 1–22 (2015).
- <sup>38</sup>V. Pasquariello, G. Hammerl, F. Örley, S. Hickel, C. Danowski, A. Popp, W. A. Wall, and N. A. Adams, "A cut-cell finite volume-finite element coupling approach for fluid-structure interaction in compressible flow," *J. Comput. Phys.* **307**, 670–695 (2016).
- <sup>39</sup>T. J. Poinso and S. K. Lele, "Boundary conditions for direct simulations of compressible viscous flows," *J. Comput. Phys.* **101**, 104–129 (1992).
- <sup>40</sup>Z.-T. Xie and I. P. Castro, "Efficient generation of inflow conditions for large eddy simulation of street-scale flows," *Flow. Turbul. Combust.* **81**, 449–470 (2008).
- <sup>41</sup>L. Laguarda and S. Hickel, "Analysis of improved digital filter inflow generation methods for compressible turbulent boundary layers," *Comput. Fluids* **268**, 106105 (2023).
- <sup>42</sup>S. Pirozzoli and M. Bernardini, "Turbulence in supersonic boundary layers at moderate Reynolds number," *J. Fluid Mech.* **688**, 120–168 (2011).
- <sup>43</sup>H. M. Hilber, T. J. Hughes, and R. L. Taylor, "Improved numerical dissipation for time integration algorithms in structural dynamics," *Earthquake Eng. Struct. Dyn.* **5**, 283–292 (1977).
- <sup>44</sup>N. M. Newmark, "A method of computation for structural dynamics," *J. Engrg. Mech. Div.* **85**, 67–94 (1959).
- <sup>45</sup>E. H. Dowell and K. C. Hall, "Modeling of fluid-structure interaction," *Annu. Rev. Fluid Mech.* **33**, 445 (2001).
- <sup>46</sup>J. M. Dickens, J. M. Nakagawa, and M. J. Wittbrodt, "A critique of mode acceleration and modal truncation augmentation methods for modal response analysis," *Comput. Struct.* **62**, 985–998 (1997).
- <sup>47</sup>M. P. Simens, J. Jiménez, S. Hoyas, and Y. Mizuno, "A high-resolution code for turbulent boundary layers," *J. Comput. Phys.* **228**, 4218–4231 (2009).
- <sup>48</sup>P. Schlatter, R. Örlü, Q. Li, G. Brethouwer, J. H. M. Fransson, A. V. Johansson, P. H. Alfredsson, and D. S. Henningson, "Turbulent boundary layers up to  $Re_\theta = 2500$  studied through simulation and experiment," *Phys. Fluids* **21**, 051702 (2009).
- <sup>49</sup>J. Sillero, J. Jiménez, R. D. Moser, and N. P. Malaya, "Direct simulation of a zero-pressure-gradient turbulent boundary layer up to  $Re_\theta = 6650$ ," *J. Phys.: Conf. Ser.* **318**, 022023 (2011).
- <sup>50</sup>K. E. Schoenherr, "Resistance of flat surfaces moving through a fluid," *Trans. Soc. Nav. Archit. Mar. Eng.* **40**, 279–313 (1932).
- <sup>51</sup>A. J. Smits, N. Matheson, and P. N. Joubert, "Low-Reynolds-number turbulent boundary layers in zero and favorable pressure gradients," *J. Ship Res.* **27**, 147–157 (1983).
- <sup>52</sup>E. R. Van Driest, *The Problem of Aerodynamic Heating* (Institute of the Aeronautical Sciences, 1956).
- <sup>53</sup>V. Pasquariello, M. Grilli, S. Hickel, and N. A. Adams, "Large-eddy simulation of passive shock-wave/boundary-layer interaction control," *Int. J. Heat Fluid Flow* **49**, 116–127 (2014).
- <sup>54</sup>J. Dély, J. G. Marvin, and E. Reshotko, "Shock-wave boundary layer interactions," NATO Technical Report No. AGARD-AG-280 (1986).
- <sup>55</sup>S. Pirozzoli and F. Grasso, "Direct numerical simulation of impinging shock wave/turbulent boundary layer interaction at  $M = 2.25$ ," *Phys. Fluids* **18**, 065113 (2006).
- <sup>56</sup>J. Fang, A. A. Zheltovodov, Y. Yao, C. Moulinec, and D. R. Emerson, "On the turbulence amplification in shock-wave/turbulent boundary layer interaction," *J. Fluid Mech.* **897**, A32 (2020).
- <sup>57</sup>P. J. Schmid, "Dynamic mode decomposition of numerical and experimental data," *J. Fluid Mech.* **656**, 5–28 (2010).
- <sup>58</sup>T. Sayadi and P. J. Schmid, "Parallel data-driven decomposition algorithm for large-scale datasets: With application to transitional boundary layers," *Theor. Comput. Fluid Dyn.* **30**, 415–428 (2016).
- <sup>59</sup>M. R. Jovanović, P. J. Schmid, and J. W. Nichols, "Sparsity-promoting dynamic mode decomposition," *Phys. Fluids* **26**, 024103 (2014).
- <sup>60</sup>L. Laguarda, S. Hickel, F. F. J. Schrijer, and B. W. van Oudheusden (2023). "Supplementary material to the publication 'Shock-wave/turbulent boundary-layer interaction with a flexible panel,'" 4TU.Researchdata. Version 1, Dataset. <https://doi.org/10.4121/01bb5a10-aa50-4ac9-b638-ec57937e27a9>
- <sup>61</sup>S. Priebe, J. H. Tu, C. W. Rowley, and M. P. Martín, "Low-frequency dynamics in a shock-induced separated flow," *J. Fluid Mech.* **807**, 441–477 (2016).
- <sup>62</sup>J.-P. Dussauge, P. Dupont, and J.-F. Debiève, "Unsteadiness in shock wave boundary layer interactions with separation," *Aerosp. Sci. Technol.* **10**, 85–91 (2006).
- <sup>63</sup>S. Priebe and M. P. Martín, "Low-frequency unsteadiness in shock wave-turbulent boundary layer interaction," *J. Fluid Mech.* **699**, 1–49 (2012).